Cell Reports

Article

The spinal premotor network driving scratching flexor and extensor alternation

Graphical abstract

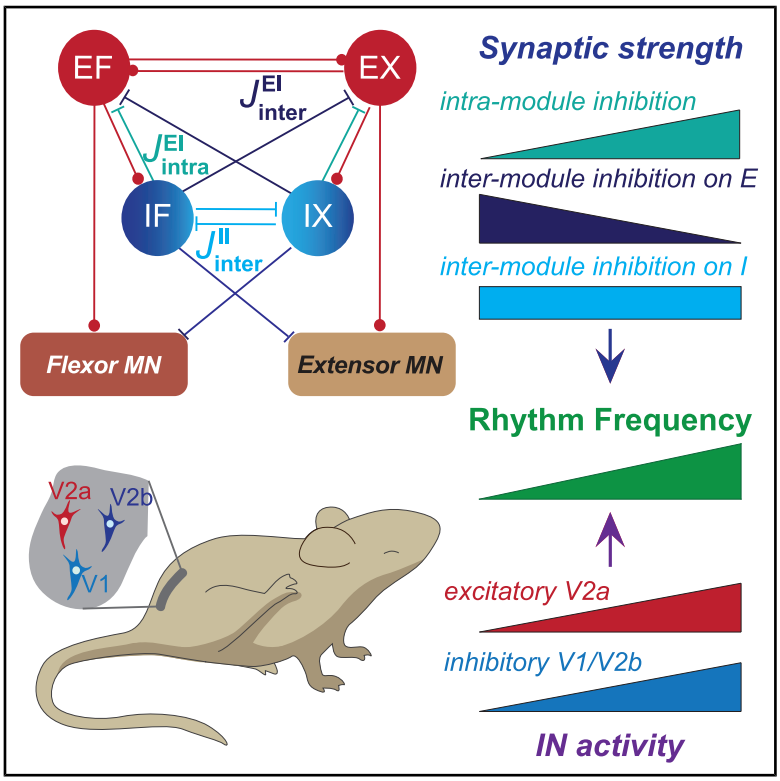

Highlights

- Excitatory V2a and inhibitory V1 and V2b neurons cooperate to generate rhythm
- Distinct inhibitory synapses differentially modulate rhythm
- Intra-module inhibition modulates adaptation currents in V2a neurons to set rhythm
- V1, V2a, and V2b neurons act synergistically and redundantly in fast rhythmogenesis

Authors

Mingchen Yao, Akira Nagamori, Sandrina Campos Maçãs, ..., Martyn Goulding, David Golomb, Graziana Gatto

Correspondence

eazim@salk.edu (E.A.), sharpee@salk.edu (T.S.), goulding@salk.edu (M.G.), golomb@bgu.ac.il (D.G.), graziana.gatto@uk-koeln.de (G.G.)

In brief

Yao et al. developed a neuromechanical model based on experimental perturbations, aligning theory-predicted with genetically labeled cell types. This work highlights the importance of inhibitory interactions within oscillatory modules, providing a template that can serve as a building block beyond scratching, e.g., for locomotion, and beyond the rodent spinal cord.

Yao et al., 2025, Cell Reports *44*, 115845
June 24, 2025
https://doi.org/10.1016/j.celrep.2025.115845

CellPress

Cell Reports

CellPress
OPEN ACCESS

Article

The spinal premotor network driving scratching flexor and extensor alternation

Mingchen Yao,[1,2] Akira Nagamori,[3] Sandrina Campos Maçãs,[4] Eiman Azim,[3,*] Tatyana Sharpee,[1,2,*] Martyn Goulding,[3,*] David Golomb,[5,6,*] and Graziana Gatto[4,7,*]

[1]Computational Neurobiology Laboratory, Salk Institute for Biological Studies, La Jolla, CA, USA
[2]Department of Physics, UCSD, La Jolla, CA, USA
[3]Molecular Neurobiology Laboratory, Salk Institute for Biological Studies, La Jolla, CA, USA
[4]Clinic and Policlinic for Neurology, University Hospital Cologne, Cologne, Germany
[5]Departments of Physiology and Cell Biology and Physics, Ben Gurion University, Be′er-Sheva 8410501, Israel
[6]School of Brain Sciences and Cognition, Ben Gurion University, Be′er-Sheva 8410501, Israel
[7]Lead contact
*Correspondence: eazim@salk.edu (E.A.), sharpee@salk.edu (T.S.), goulding@salk.edu (M.G.), golomb@bgu.ac.il (D.G.), graziana.gatto@uk-koeln.de (G.G.)
https://doi.org/10.1016/j.celrep.2025.115845

SUMMARY

Rhythmic motor behaviors are generated by neural networks termed central pattern generators (CPGs). Although locomotor CPGs have been extensively characterized, it remains unknown how the neuronal populations composing them interact to generate adaptive rhythms in mammals. We explored the cooperation dynamics among the three main populations of ipsilaterally projecting spinal CPG neurons—V1, V2a, and V2b neurons—in scratch reflex rhythmogenesis. Individual ablation of the three neuronal populations reduced the oscillation frequency. Activation of excitatory V2a neurons enhanced the oscillation frequency, while activating inhibitory V1 neurons suppressed movement. Building on these findings, we developed a neuromechanical model made of self-oscillating flexor and extensor modules coupled via inhibition. Rhythm frequency is increased by strong intra-module inhibition and facilitation mechanisms in excitatory neurons and decreased by strong inter-module inhibition. In sum, we describe how genetically identified neuron types and the strengths of their synaptic connections drive scratch rhythmogenesis.

INTRODUCTION

The variety of rhythmic behaviors across species suggests evolution has selected diverse mechanisms of rhythmogenesis. Yet, the molecular, cellular, and circuit dynamics underlying this diversity of rhythms remain poorly understood. Conserved neuronal networks in the spinal cord, termed central pattern generators (CPGs), produce a range of rhythmic behaviors, like swimming, walking, and scratching, by shaping the timing and coordination patterns of limb and appendicular muscle contractions.[1,2]

Locomotion has long been the model behavior to study rhythmogenesis and its underlying cellular and circuit components. Locomotor rhythm is primarily generated by excitatory neurons and/or neural networks with intrinsic bursting properties.[3] Spinal CPGs comprise six genetically identified populations—dI6, V0, V1, V2a, V2b, and V3 neurons—differing in axonal projection patterns and neurotransmitter phenotypes.[1] Rhythmogenic neurons are primarily ipsilaterally projecting such that each hemicord generates rhythmic activity.[2] Excitatory Chx10-expressing V2a neurons (Chx10-V2a) set locomotor speed in zebrafish[4] but not in rodents,[5–7] likely due to compensation from Shox2-expressing V2a (Shox2-V2a),[7] V3,[8] and the non-canonical CPG Hb9-expressing neurons.[9] The role of inhibition in rhythmogenesis is less clear. Loss of inhibitory V1 neurons slows down the *in vitro* locomotor rhythm in mice[10,11] and swimming in zebrafish[12] and tadpoles.[13] By contrast, ablation of inhibitory V2b neurons accelerates swimming in zebrafish,[14] but has no effects on rhythm in mice.[15] Despite progress in identifying the role of individual populations in rhythmogenesis, it remains unclear how excitatory and inhibitory neurons interact to generate rhythmic behaviors.

Classic models of locomotor rhythmogenesis[16–18] have coalesced around the half-center model, in which rhythm is driven by the inhibitory coupling of flexor and extensor modules.[19,20] In alternative models, locomotor rhythm arises from individual modules acting as intrinsic bursting oscillators.[3] However, it remains unclear whether these mechanisms apply to faster rhythms. Since limbed animals adapt to higher locomotor speeds not only by increasing frequency but also by changing their gait,[5,21–24] we focused on a simpler rhythmic behavior, the scratch reflex.[25] Scratching is faster than walking and entails unilateral and mostly mono-articular oscillations,[26] allowing us to focus on how ipsilaterally projecting excitatory V2a and inhibitory V1 and V2b neurons contribute to faster rhythm generation.

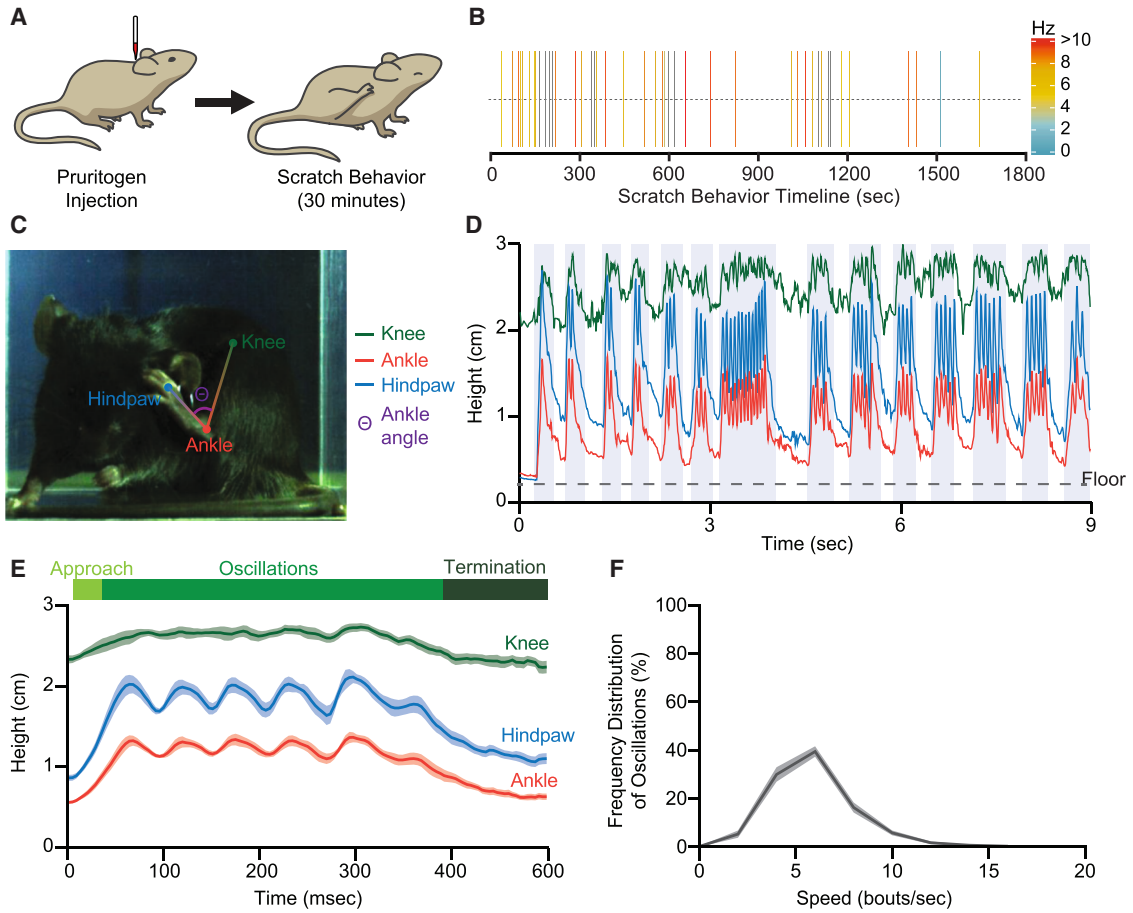

Figure 1. Kinematic analysis of the scratch reflex

(A) Schematic illustrating chloroquine injection-induced scratching.

(B) Raster plot showing the variability in oscillation frequency during scratching in a wild-type mouse. Oscillation frequency of each episode is color-coded as in the legend.

(C) Snapshot of a mouse scratching with tracked knee (green), ankle (orange), and hindpaw (azure) landmarks, and ankle angle θ (purple).

(D and E) Changes in knee (green), ankle (orange) and hindpaw (azure) height. Individual scratch episodes are labeled with gray rectangles in (D). Episodes with similar frequency (N = 10, from three mice) were chosen and averaged in (E).

(F) Frequency distributions of the speed of oscillations (bouts/second) of all scratch episodes, N = 30 mice. A bout is defined as one circular trajectory around the nape (one oscillation).

Data presented as mean ± SEM, SEM represented as shaded area. See also Figure S1.

We found that individual ablation of either excitatory or inhibitory neurons reduced the scratch oscillation frequency. Activation of excitatory V2a neurons increased the scratch rhythm, while activating inhibitory V1 neurons suppressed spontaneous movements. To mechanistically assess how excitatory and inhibitory neurons cooperate to generate rhythms, we developed a neuromechanical model, made of two self-oscillating flexor and extensor modules coupled via inhibition. Analyses of our model showed that rhythm is accelerated via stronger intra-module inhibition and facilitation mechanisms in excitatory synapses, and slowed down by stronger inter-module inhibition. In sum, combining computational and experimental approaches we provide a mechanistic description of the cooperation dynamics of excitatory and inhibitory neurons underlying fast rhythmogenesis.

RESULTS

Kinematic analysis of the scratch reflex

Scratching is an evolutionary conserved reflex, executed as a stereotypical sequence of high-frequency hindlimb oscillations.[25] Injecting chloroquine, a pruritogen, into the nape of mice (Figure 1A) resulted in sustained scratching, which occurred in multiple episodes of varying duration and frequency (Figures 1B–1D and S1A; Video S1). Individual scratch episodes comprised three phases: approach, rhythmic oscillations, and termination. The hindlimb is initially flexed toward the trunk (approach), then rhythmically extended and flexed around the nape (oscillations), and finally extended back toward the floor (termination) (Figure 1E). Kinematic tracking showed that mice predominantly scratch using the distal limb (Figure 1E), primarily by generating rhythmic ankle oscillations (Figure S1B). The limb

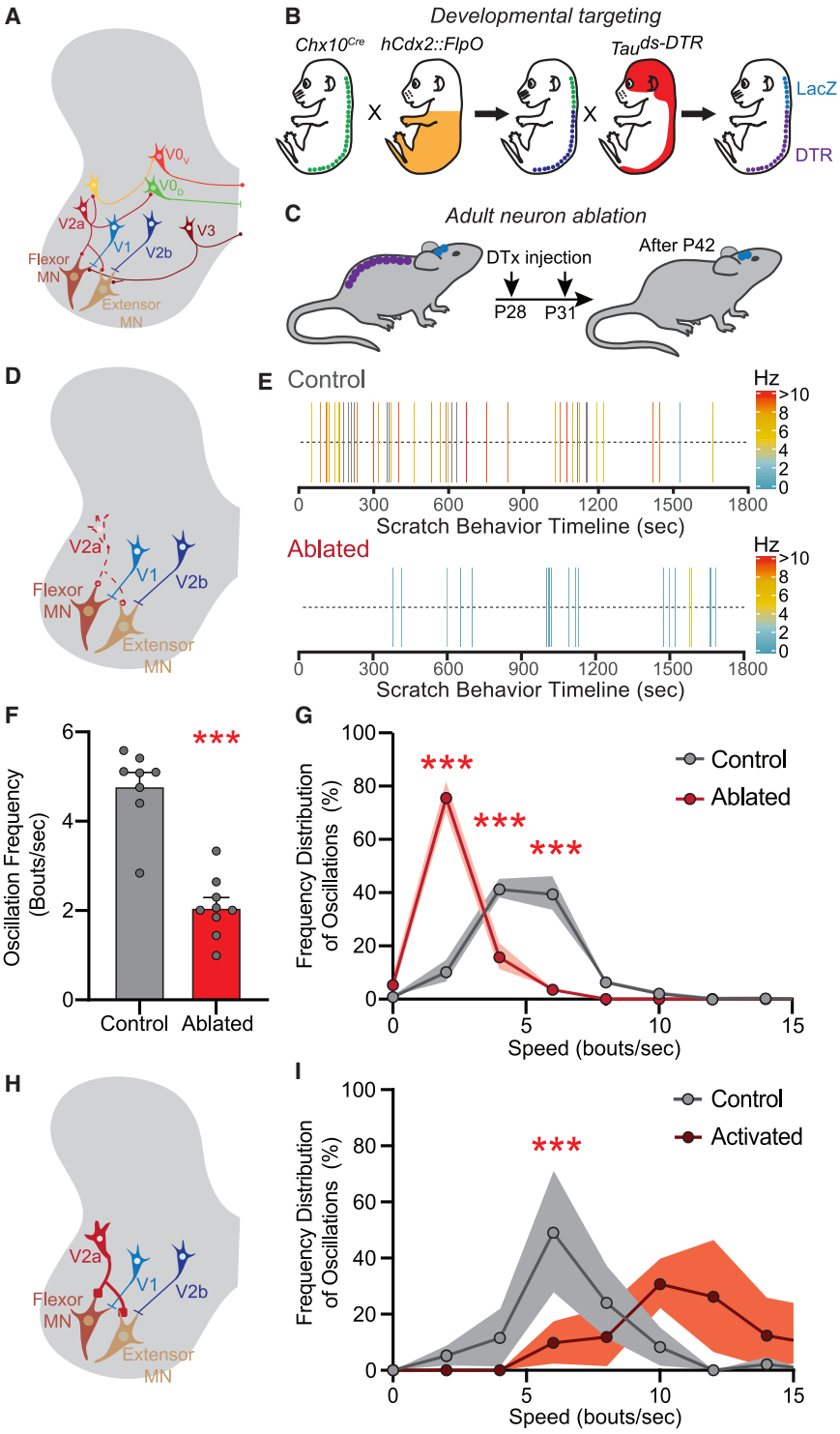

Figure 2. Ipsilateral excitatory V2a neurons drive high-frequency scratch oscillations

(A–C, D, and H) Schematics illustrating the CPG neuronal populations (MN: motoneurons) (A), the intersectional approach to drive DTR expression (Tau^{ds-DTR}) in spinal excitatory V2a neurons (B), the timeline of ablation and behavioral testing (C), and the ablation (D) and the CNO-driven activation (H) of V2a neurons.

(E) Ablation of V2a neurons impairs the scratch response. Frequency of oscillations of each episode is color-coded as in the legend.

(F) Ablation of V2a neurons reduces the average oscillation frequency. Statistical analysis: two-tailed Student's t test, $^{***}p < 0.0001$.

(G) Ablation of V2a neurons shifts to the left (slower) the frequency distribution of the oscillation speeds (bouts/second). Controls (gray), $N = 8$, V2a neuron-ablated mice (red), $N = 9$. Statistical analysis: two-way ANOVA (interaction genotype × speed, $p < 0.0001$) with Bonferroni's post hoc test, $^{***}p < 0.0001$ for genotype comparison at 2, 4, and 6 bouts/second.

(I) CNO activation of V2a neurons (dark red, $N = 7$) shifts to the right (faster) the frequency distribution of the speeds of oscillations (bouts/second) during spontaneous scratching compared with controls (gray, $N = 4$). Statistical analysis: two-way ANOVA (interaction genotype × speed, $p = 0.0004$) with Bonferroni's post hoc test, $^{***}p < 0.0001$ for genotype comparison at 6 bouts/second.

Data presented as mean ± SEM. Individual mice represented as filled gray circles (F), SEM as shaded area (G and I). See also Figure S2.

flexion during the approach was similar across episodes and animals (Figure S1C), whereas the oscillation frequency, the duration of individual episodes, the amplitude of movements, and the termination phase were highly variable within and across trials and mice (Figures 1D, S1A, S1D, and S1E). The frequency distribution of the speeds of scratch oscillations showed that they range from 2 to 15 Hz, with a peak at 6 Hz (Figure 1F). These analyses showed that scratching is a unilateral movement driven by ankle oscillations over a range of frequencies, validating it as an experimentally accessible model to study rhythmogenesis.

Ipsilateral excitatory V2a neurons drive the high-frequency scratch oscillations

The excitatory V2a and the inhibitory V1 neurons (Figure 2A) showed increased expression of the immediate-early gene cFos[27] after scratching, suggesting they play an active role in its execution (Figure S2A). Thus, we decided to focus on the ipsilaterally projecting populations. We perturbed the activity of V1, V2a, and V2b neurons using an intersectional genetic approach that combines the *hCdx2::FlpO* allele to restrict expression to the spinal cord,[15] with selected *Cre* lines that developmentally capture these neuronal lineages (Figure 2B). Dual recombinase-expressing mice were then crossed with animals carrying *Cre*- and *Flp*-dependent effectors: the diphtheria toxin receptor

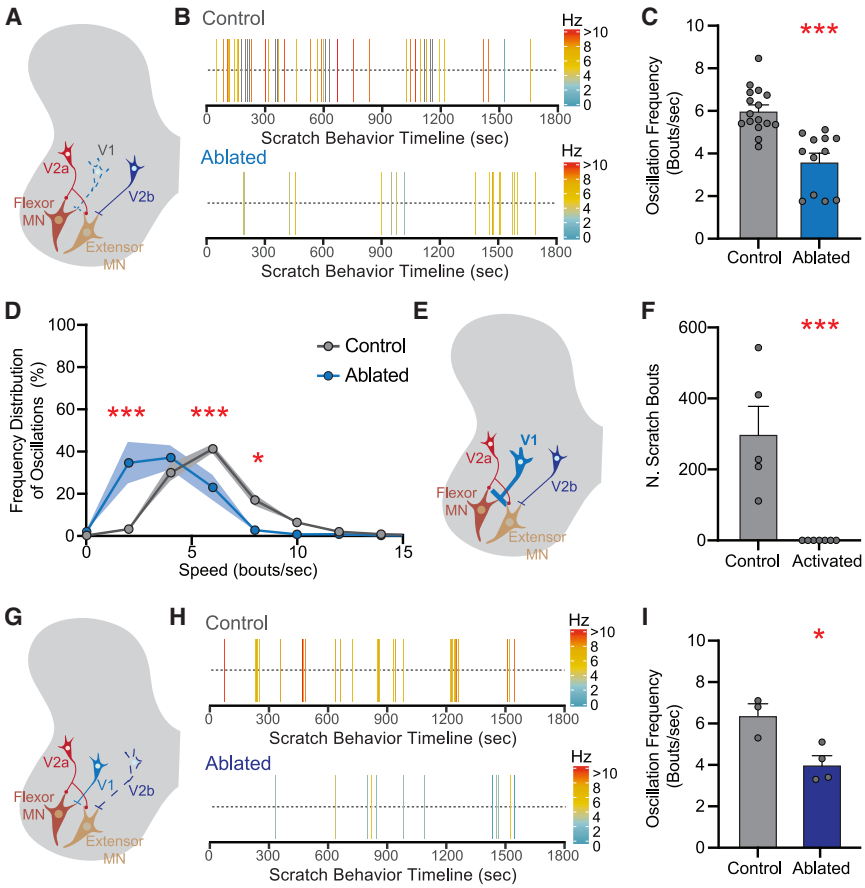

Figure 3. Ipsilateral inhibitory neurons modulate the frequency of scratch oscillations

(A, E, and G) Schematics illustrating the ablation of V1 (A) and V2b neurons (G) and the CNO-driven activation of V1 neurons (E).

(B and H) Ablation of V1 (B) and V2b neurons (H) impairs the scratch response. Frequency of oscillations of each episode is color-coded as in the legend.

(C and I) Ablation of V1 (C) and V2b (I) neurons reduces the average oscillation frequency, $^{***}p < 0.0001$ (V1), $^{*}p = 0.0178$ (V2b).

(D) Ablation of V1 neurons shifts to the left (slower) the frequency distribution of the oscillation speeds (bouts/second). Controls (gray), $N = 16$, V1 neuron-ablated mice (cerulean), $N = 12$. SEM represented as shaded area. Statistical analysis: two-way ANOVA (interaction genotype × speed, $p < 0.0001$) with Bonferroni's post hoc test, genotype comparison $^{***}p < 0.0001$ at 2 bouts/second, $^{***}p = 0.0004$, at 6 bouts/second, $^{*}p = 0.0105$ at 8 bouts/second.

(F) CNO-driven activation of V1 neurons induces an atonia-like state, $^{***}p = 0.0009$.

Data presented as mean ± SEM. Individual mice represented as filled gray circles. Statistical analysis: two-tailed Student's t test, unless otherwise indicated. See also Figure S3.

(DTR) allele ($Tau^{ds\text{-}DTR}$)[15] for neuronal ablation, the hM4Di DREADD ($R26^{ds\text{-}hM4Di}$)[28] for transient silencing, and the hM3Dq DREADD ($R26^{ds\text{-}hM3Dq}$)[29] for transient activation. Importantly, as the ligands for these receptors were only administered in adult mice, this strategy allowed for normal development of the spinal circuits.

Excitatory V2a neurons were ablated by diphtheria toxin (DTx) injection in adult mice (Figures 2B and 2C), with littermates lacking the *FlpO* allele used as controls. Ablating V2a neurons (Figures 2D and S2B) significantly reduced the scratch oscillation frequency (Figures 2E and 2F) and the number of scratch bouts (Figure S2C). The frequency distribution analysis of all scratch episodes showed a marked shift toward slower oscillations (Figure 2G). To exclude that these results were due to post-ablation re-organization of the CPG circuitry or compensation, we performed acute silencing experiments using the inhibitory DREADD hM4Di (Figure S2D). Clozapine N-oxide (CNO)-driven silencing of the V2a neurons slowed down the oscillation frequency (Figures S2E–S2G), phenocopying the ablation results (Figures 2E–2G).

Finally, we performed acute activation experiments using the excitatory DREADD hM3Dq (Figures 2H and S2H). CNO-driven activation of V2a neurons induced faster oscillations (Figures 2I and S2J), without affecting the number of scratch bouts (Figure S2I). Taken together, our data show that V2a neuron ablation or silencing slows down the scratch rhythm, whereas V2a neuron activation accelerates it.

Ipsilateral inhibitory neurons modulate the frequency of scratch oscillations

To assess how inhibitory neurons contribute to rhythmogenesis, we targeted the main source of ipsilateral inhibition onto limb motoneurons, V1 and V2b neurons.[30] We used mice expressing the *hCdx2::FlpO* and $En1^{Cre}$ alleles to restrict DTR expression to V1 neurons,[15] and littermates lacking *FlpO* as controls. Ablating V1 neurons (Figures 3A and S3A) decreased the oscillation frequency (Figures 3B–3D) and the number of scratch bouts (Figure S3B). CNO-driven silencing of V1 neurons via hM4Di (Figure S3C) recapitulated the ablation phenotype (Figures S3D–S3F), excluding it from being due to ablation-induced re-wiring or compensation. CNO activation of V1 neurons via hM3Dq (Figure 3E) resulted in an atonia-like state, with no spontaneous movements observed until drug wash-out (Figure 3F).

We used $Hes2^{iCre}$ that labels all V2 neurons[31] and $VGAT^{FlpO}$ that targets inhibitory neurons to restrict DTR expression to V2b neurons. Ablation of V2b neurons (Figures 3G and S3G) significantly reduced the oscillation frequency (Figures 3H, 3I, and S3I), with no changes in number of scratch bouts (Figure S3H). Taken together, our findings show that the

inhibitory V1 and V2b neurons play a critical role in sustaining faster scratch oscillation frequencies.

Neural model of scratch rhythmogenesis

To mechanistically understand how excitatory and inhibitory neurons cooperate to generate rhythm, we developed a novel neuromechanical model that investigates the dynamics underlying (1) the slower rhythm induced by ablation of excitatory V2a neurons (Figures 2F and 2G), (2) the faster rhythm due to activation of excitatory V2a neurons (Figures 2I and S2J), (3) the slower rhythm caused by ablation of inhibitory V1 and V2b neurons (Figures 3C, 3D, 3I, and S3I), and (4) the atonia driven by inhibitory V1 neuron activation (Figure 3F).

Our model of scratch rhythmogenesis is based on the population average, with intrinsic and synaptic variables representing populations rather than individual neurons (STAR Methods). We opted for a rate model, as it allows us to simplify conductance-based models by assuming constant or slowly varying inputs and asynchronous firing.[32] This permits the use of simplified schemes to compute circuit dynamics and characterize their underlying mechanisms.[33–35] The model (Figure 4A) was built on four assumptions. First, it comprises two modules, flexor (F) and extensor (X), coupled via inhibition. Each module includes three populations: excitatory (E), inhibitory (I), and motoneurons (M). Flexor motoneurons (MF) are innervated by excitatory flexor neurons (EF) and inhibitory extensor neurons (IX). Extensor motoneurons (MX) receive mirrored input. Second, the excitatory neuronal populations in each module (EF and EX) generate rhythmic activity by network bursting, due to adaptation and intrinsic depolarization currents in V2a neurons. Third, the frequency of rhythmic bursting is modulated by recurrent intra-module excitatory-to-inhibitory connections. Fourth, excitatory neurons have facilitation mechanisms, as facilitation modulates the oscillation frequency in networks with bursting neurons.[36–38]

V2a neurons are symmetrically represented in the EX and EF populations, since V2a neurons equally innervate flexor and extensor motoneurons.[39–41] Since ablating Chx10-V2a neurons did not completely abolish the rhythm (Figures 2F and 2G), the E populations include an additional rhythmogenic excitatory neuron type, analogous to Shox2-V2a or V3 neurons.[7,8] The neurons in the I populations are not intrinsically bursting but have adaptation currents. V1 and V2b neurons are asymmetrically distributed in the IX and IF populations to reflect their anatomical bias in flexor and extensor motoneuron innervation,[15] with V1 neurons preferentially contributing to the IX population, and V2b neurons to the IF population (Figures 4A and S4A). As V1 neurons are twice as abundant as V2b neurons (U19-SCC, unpublished data), they account for a higher total fraction of I neurons (Figure S4A). The strength of synaptic connectivity between two neuronal populations is represented by the synaptic coupling conductance (J), separated into intra- (J_{intra}) or inter-module (J_{inter}), and differentiated based on the post- and presynaptic neurons (STAR Methods).

Biomechanical model of single joint oscillations

Muscles represent a fundamental filter of neuronal activity, being the ultimate checkpoint between motoneuron firing and biomechanical actuation.[42,43] Thus, we developed a biomechanical model to enable a better comparison between the output of our neural model and the behavioral responses observed. We modeled the ankle joint as a one degree of freedom, two-link segment model, in which only the distal segment can rotate around an axis in the fixed proximal segment (Figure 4B). The distal segment is actuated by an antagonistic pair of identical muscles (flexor and extensor), connecting the proximal and distal segments in a bow-string configuration (Figure 4B). We used a Hill-type muscle model to convert motoneuron activity into muscle force, taking into account the muscle low-pass filtering effects, the length-dependent muscle activation, the force-length relationship, and a passive elastic element (Figure S7, STAR Methods).

Increases in inhibition or excitation within a single module drive faster motoneuron bursting

First, we analyzed the dynamics in a single module (Figure 4C). Rhythmic bursting of motoneurons (M) is driven by the bursting excitatory population (E) activated by an excitatory tonic input (Figures S4B and S4C). Firing of inhibitory neurons (I) is elicited by the E neurons during their active phase and contributes to the termination of E neuron bursting (Figure 4C). At the end of the E neuron bursting, the adaptation current begins to decay, with the latency of decay determined by the beginning of the next active phase (Figure S4D). Strengthening the I-to-E inhibitory conductance (J^{EI}) reduces the firing rate (r) of E neurons, leading to a weaker adaptation current and a shorter latency of its decay. The reduced latency of decay causes the faster onset of a new active phase, thus effectively increasing motoneuron bursting frequency (Figures 4D and S4E). Similar increases in frequency are observed for strong E-to-I excitatory conductance (J^{IE}) (Figure S4F). Thus, within a single module the frequency of motoneuron bursting is dictated by the activity of the E and I populations and the strength of their synaptic connections.

The differential contribution of intra- and inter-module inhibition to rhythmogenesis

Our model comprises three types of inhibitory synapses: (1) inter-module I-to-I inhibition (J^{II}_{inter}), (2) inter-module I-to-E inhibition (J^{EI}_{inter}), and (3) intra-module I-to-E inhibition (J^{EI}_{intra}) (Figure 4A). To examine how each inhibitory synapse type contributes to rhythmogenesis, we evaluated how the oscillation frequency changes as a function of their strength. The oscillation frequency is almost unaffected by changing the strength of inter-module I-to-I inhibition (Figure 4E), and increases with weaker inter-module I-to-E inhibition (Figure S4G). By contrast, the oscillation frequency decreases with weaker intra-module I-to-E inhibition (Figure 4F), consistent with the single module results (Figure 4D). As reducing the strength of inter- and intra-module I-to-E inhibition has opposite effects on the frequency of motoneuron bursting, the net effect of reducing inhibition in the entire circuit depends on the relative strengths of the individual synapses. For example, reducing overall inhibition decreases frequency for small values of inter-module I-to-E inhibition (J^{EI}_{inter} 70–100 $\mu A/cm^2$), while increases it for larger values (J^{EI}_{inter} 250 $\mu A/cm^2$) (Figure S4H). The strength of inter-module I-to-I inhibition does not affect how reducing overall inhibition impacts rhythm (Figure S4I). In sum, individual inhibitory synapses play distinct

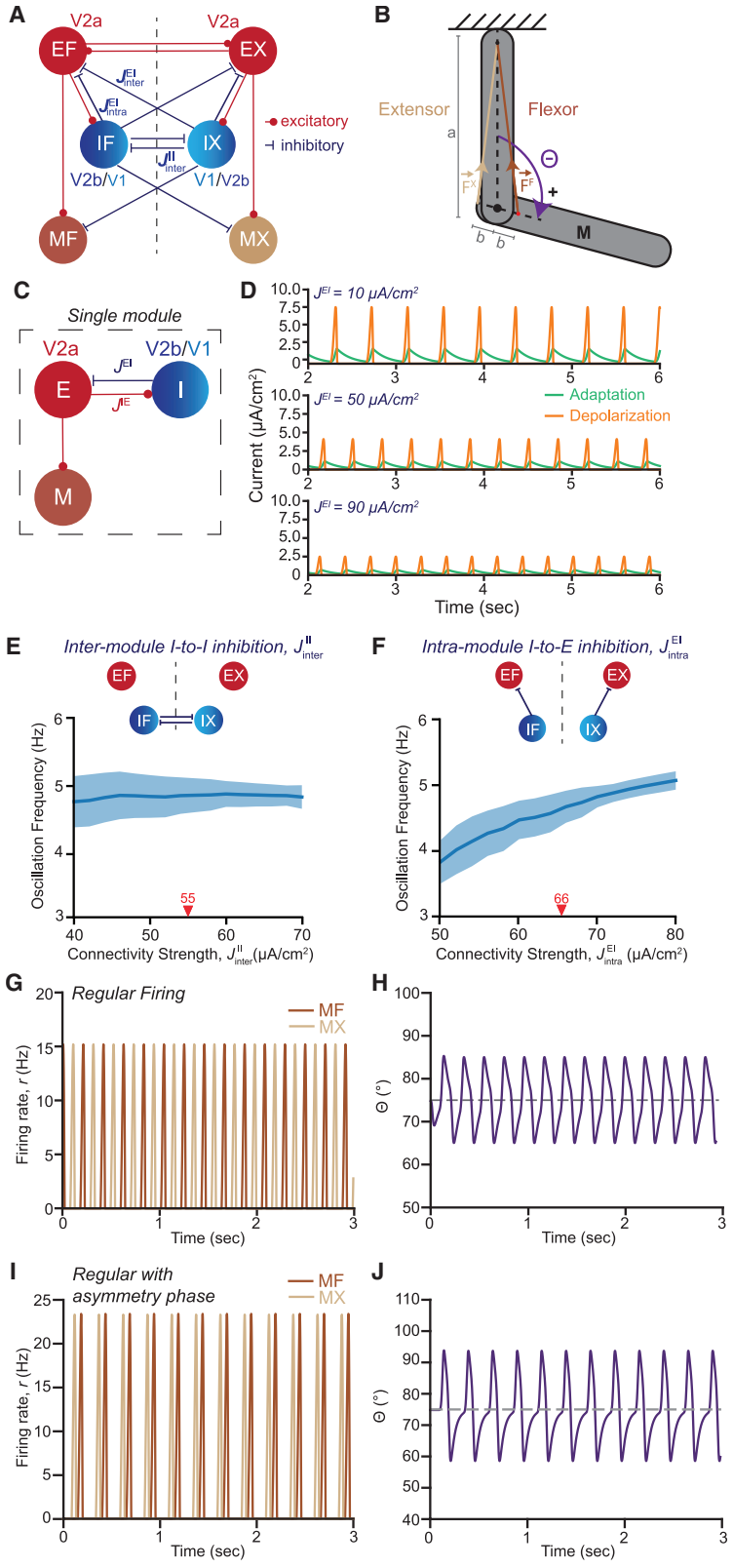

Figure 4. Neuromechanical model of scratch rhythmogenesis

(A–C) Schematics illustrating the architecture of the full neural model (A), the single module model (C), and the biomechanical model (B).

(D) Strengthening the I-to-E inhibitory conductance increases the oscillation frequency, as shown by the simulated time traces of the intrinsic adaptation and depolarization currents for three distinct strengths of I-to-E inhibitory conductance.

(E and F) The oscillation frequency of the neuromechanical model is not affected by the strength of the inter-module I-to-I inhibition (E) but varies as a function of the strength of the intra-module I-to-E inhibition (F). Red arrowheads and numbers indicate the values of synaptic strength used as reference parameters in our model (Table 1). Data presented as mean ± SD of 50 realizations of synaptic conductance parameters, SD represented as shaded area.

(G–J) Simulated firing rates of flexor (MF) and extensor motoneurons (MX) (G and I) and joint angle θ (H and J) generated by the neuromechanical model using the reference parameter set (Table 1) (G and H), and when 20% of V1 neurons are ablated (p^{V1} = 0.2) (I and J). See also Figure S4 and S7, and Tables 1 and 2.

roles in rhythmogenesis, with the oscillation frequency determined by their relative strengths.

In classic CPG models, the dominant inhibitory connections are the ones between "rhythm generators,"[3,44] represented here by inter-module inhibition. To generate bursting, each "rhythm generator" needs at least one slow variable, e.g., an activation variable of a hyperpolarizing conductance.[45,46] Weakening inter-module inhibition reduces the time each module spends in its passive state, making the slow variable larger at the beginning of the next active phase, thus effectively increasing frequency. This contrasts with our experimental results, as ablation of inhibitory neurons reduces frequency (Figures 3C and 3I). Thus, we propose that, during scratching, the intra-module I-to-E inhibition is the dominant inhibitory connection, as reducing its strength effectively reduces the oscillation frequency (Figure 4F).

Computed motoneuron bursting patterns following perturbations of neuron activity

To mimic experimental perturbations in our model, we computed neuronal ablation as a decrease in the total synaptic conductance output (Equations 3 and 4, STAR Methods), and activation as an increase in the input current received (Equations 5 and 6, STAR Methods). Changing the ablation efficiency, defined by the parameter p, or the activation efficiency, defined by the injected current I_{act}, varies the dynamical states of the coupled modules, resulting in different patterns of MX and MF activity. In the absence of any ablation ($p = 0$), MF and MX fire anti-synchronously (Figure 4G), driving oscillations (Figure 4H) at similar frequencies to scratching (Figure 1F). At low-efficiency ablation of V1 neurons ($p^{V1} = 0.2$), MF and MX exhibit a phase difference (ϕ) between 0 and 2π (Figure 4I), due to the asymmetrical inhibition exerted by V1 and V2b neurons onto flexor and extensor motoneurons[15] that skews MF and MX bursting (Figure 4I). Notably, regular bursting with asymmetric phase still generates fluid limb movements (Figure 4J). At high-efficiency ablation of V1 neurons ($p^{V1} = 0.8$), MF and MX fire with an irregular, non-periodic pattern, in terms of both frequency and amplitude (Figures S4J and S4K). High-efficiency ablation of both V1 and V2a neurons ($p^{V1} = p^{V2a} = 0.95$) significantly weakens the inter-module inhibition, causing simultaneous MF and MX bursting that induces a 100% co-contraction state (Figure S4L) and restricts the amplitude of movement (Figure S4M). High-efficiency activation of V1 neurons ($I^{V1}_{act} = 2$ μA/cm^2) completely suppresses motoneuron bursting (Figure S4N), causing the limb to settle into an atonia-like state (Figure S4O), as experimentally observed (Figure 3F).

Computed circuit dynamics following perturbations of individual neuronal populations

To mechanistically define how individual neuronal populations contribute to rhythmogenesis, we examined how changing the parameters in the model to mimic the experimental perturbations affects the frequency and phase difference of motoneuron bursting. Ablation of V2a neurons was modeled as a decrease in the total synaptic output of the V2a neuron subset of the E populations (p^{V2a}). As in the experiments (Figures 2F and 2G), simulated ablation of V2a neurons (Figure 5A) decreases the oscillation frequency (Figures 5B and S5A). Since V2a neurons are equally represented in the EF and EX populations, their ablation does not affect the phase difference of MF and MX activity (Figure 5B).

Ablation of V2a neurons changes rhythm frequency by reducing the intra-module E-to-I excitation conductance, J^{IE}_{intra} (Figure S5B). When intra-module excitation is reduced, rhythm considerably slows down for weak inter- and strong intra-module inhibition, and it is mildly or not affected at all for weak ($J^{EI}_{intra} = 10$ μA/cm^2) or null intra-module inhibition (Figure S5B). Thus, the extent to which reductions in intra-module excitation impact rhythm depends on the strength of intra- and inter-module I-to-E inhibition, with strong intra-module and weak inter-module inhibition being necessary to mimic our experimental results (Figures 2E–2G).

Ablation of the V1 (p^{V1}) or V2b (p^{V2b}) neuron subsets of the I populations reduces the oscillation frequency (Figures 5C, 5D, S5C, and S5D), recapitulating our experimental results (Figures 3C, 3D, 3I, and S3I). Motoneuron bursting remains regular at low-efficiency ablation, and becomes progressively irregular (Figures 5C and 5D) with larger phase differences as the ablation efficiency increases (Figures S5E and S5F). Given the asymmetrical input that V1 and V2b neurons exert on MF and MX, their ablation causes large frequency differences between the coupled modules, leading to irregular dynamics (Figures 5C and 5D).[47] Ablation of V2b neurons, even at higher efficiency, is less effective than V1 neuron ablation in causing irregular bursting (Figures 5C and 5D), as V1 neurons are more numerous and more asymmetrically distributed between the I populations (Figure S4A). The strengths of inter-module I-to-E inhibition determine the extent to which the ablation efficiency of V1 and V2b neurons affects the oscillation frequency (Figures 5E and 5F). Ablation of V1 or V2b neurons causes small reductions in oscillation frequency for strong inter-module I-to-E inhibitory conductance ($J^{EI}_{inter} = 250$ μA/cm^2), and larger decreases for weaker values (e.g., $J^{EI}_{inter} = 100$ μA/cm^2) (Figures 5E and 5F). Changes in strength of inter-module I-to-I inhibition do not affect how V1 or V2b neuron ablation efficiency impacts frequency (Figures 5G and 5H).

Activation of the V2a neuron subset in the E populations (Figure 5I) accelerates rhythm (Figures 5J and S5G), as in our experimental results (Figures 2I and S2I), via facilitation mechanisms in the E neurons (Figures S5H–S5J). Low-efficiency activation of V1 neurons ($I^{V1}_{act} \approx 0.5$ μA/cm^2) causes irregular MF and MX bursting, due to the increasing asymmetry in the inhibition exerted by the two modules (Figure 5K). High-efficiency activation of V1 ($I^{V1}_{act} > 0.8$ μA/cm^2) or V2b neurons ($I^{V2b}_{act} > 1.0$ μA/cm^2) suppresses motoneuron bursting, leading the circuit to a fixed point (Figures 5K, 5L, S5K, and S5L) that mimics the experimentally observed atonia-like state (Figure 3F).

In summary, our neuromechanical model not only recapitulates experimental perturbations but also predicts how they affect the pattern and phase differences of motoneuron bursting as a function of their efficiency (Figures 5B–5D and 5J–5L). Our analyses also show how changes in individual synaptic strengths (Figures 5E–5H and S5B) and injected currents (Figures 5J–5L,

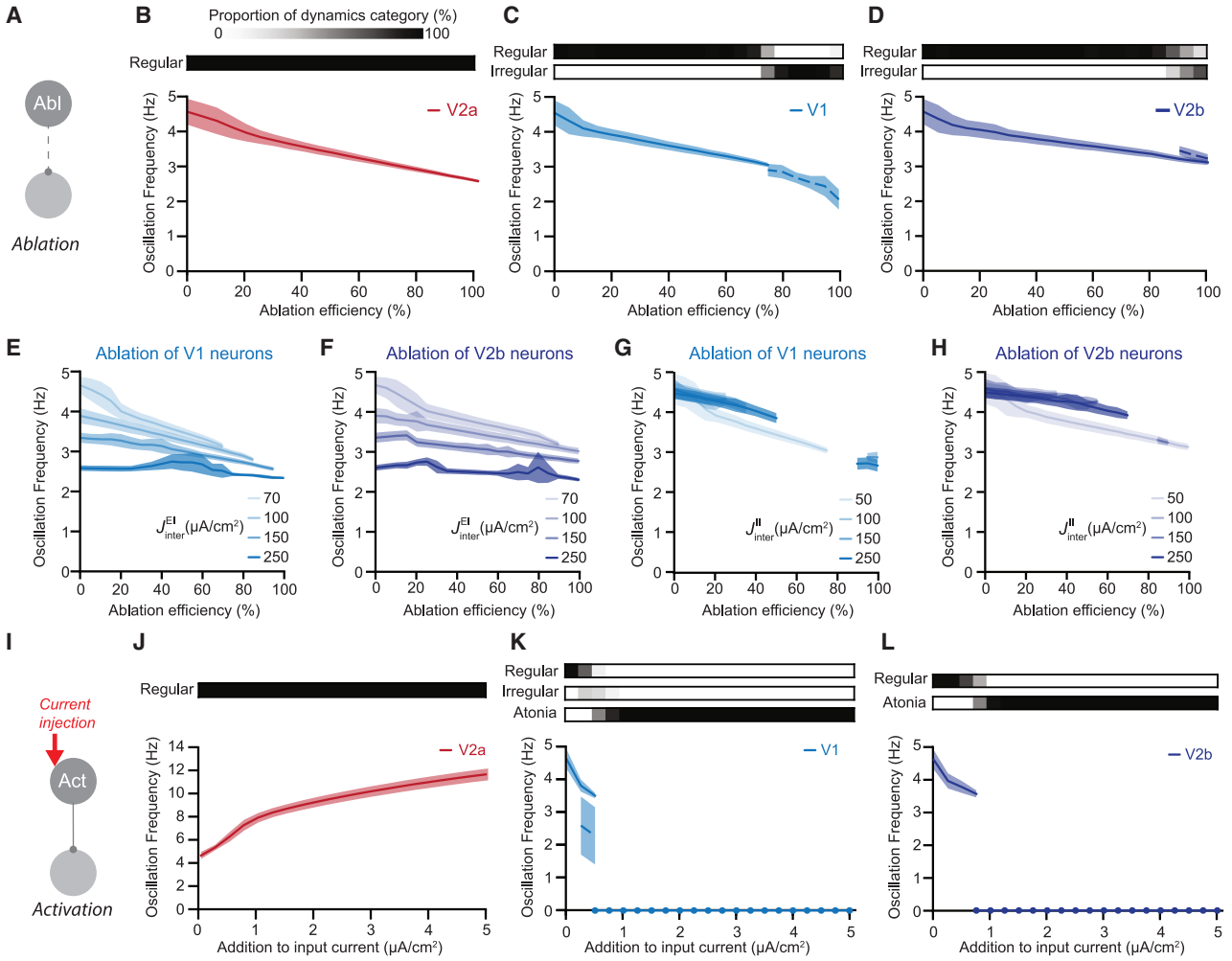

Figure 5. Computed circuit dynamics following perturbations of CPG neuronal populations

(A and I) Schematics illustrating the simulations of neuronal ablation (A) and activation (I).

(B–D) Graphs showing the computed oscillation frequency and motoneuron bursting patterns as a function of the ablation efficiency (p) of V2a (B), V1 (C), and V2b (D) neurons. The bars above the graphs represent the occurrence of distinct motoneuron bursting patterns (e.g., regular and irregular, STAR Methods) as a function of the ablation efficiency.

(E–H) Graphs showing oscillation frequency as a function of the ablation efficiency (p) of V1 (E and G) and V2b (F and H) neurons and of the strength of inter-module I-to-E inhibition (E and F) and I-to-I inhibition (G and H). These plots include only results for regular oscillations.

(J–L) Graphs showing the computed oscillation frequency and motoneuron bursting patterns as functions of the injected current in V2a (J), V1 (K), and V2b (L) neurons. The bars above the graphs represent the occurrence of motoneuron bursting patterns as a function of the input current.

Solid and dashed lines represent regular and irregular oscillations, respectively. Filled circles indicate atonia. Data presented as mean ± SD of 50 realizations of synaptic conductance parameters, SD represented as shaded area. See also Figure 5.

S5G, S5K, and S5L) modulate the effects that distinct perturbations exert on rhythm.

Rhythm frequency is controlled by distinct cooperation dynamics among the ipsilateral neuron populations

Next, we investigated how excitatory and inhibitory neurons cooperate to drive rhythm by simultaneously perturbing excitatory V2a and inhibitory V2b neurons (*Hes2*^{iCre}*;hCdx2::FlpO*)[31] or inhibitory V1 and excitatory V2a neurons (*En1*^{Cre}*;Chx10*^{Cre}*; hCdx2::FlpO*).

The co-ablation of excitatory V2a and inhibitory V2b neurons (Figures 6A and S6A) reduced the oscillation frequency (Figure 6B) and the number of scratch bouts (Figure S6B) to the same extent as individual ablation of V2a neurons. Simulations of this dual manipulation recapitulate the reduction in frequency (Figures 6C, S6C, and S6D). High-efficiency ablation of V2a and V2b neurons ($p^{V2a} = p^{V2b} = 0.95$) makes MX and MF fire in irregular patterns (Figure 6C), as observed following ablation of V2b (Figure 5D) but not V2a neurons (Figure 5B). Intriguingly, intermediate efficiency ablation ($p^{V2a} = p^{V2b} = 0.7$) of V2a and V2b neurons causes an irregular pattern, not seen following either V2a or V2b neuron ablation alone (Figure 6C). In sum, V2a and V2b neurons play partly redundant roles, as the decrease in oscillation frequency induced by their simultaneous ablation

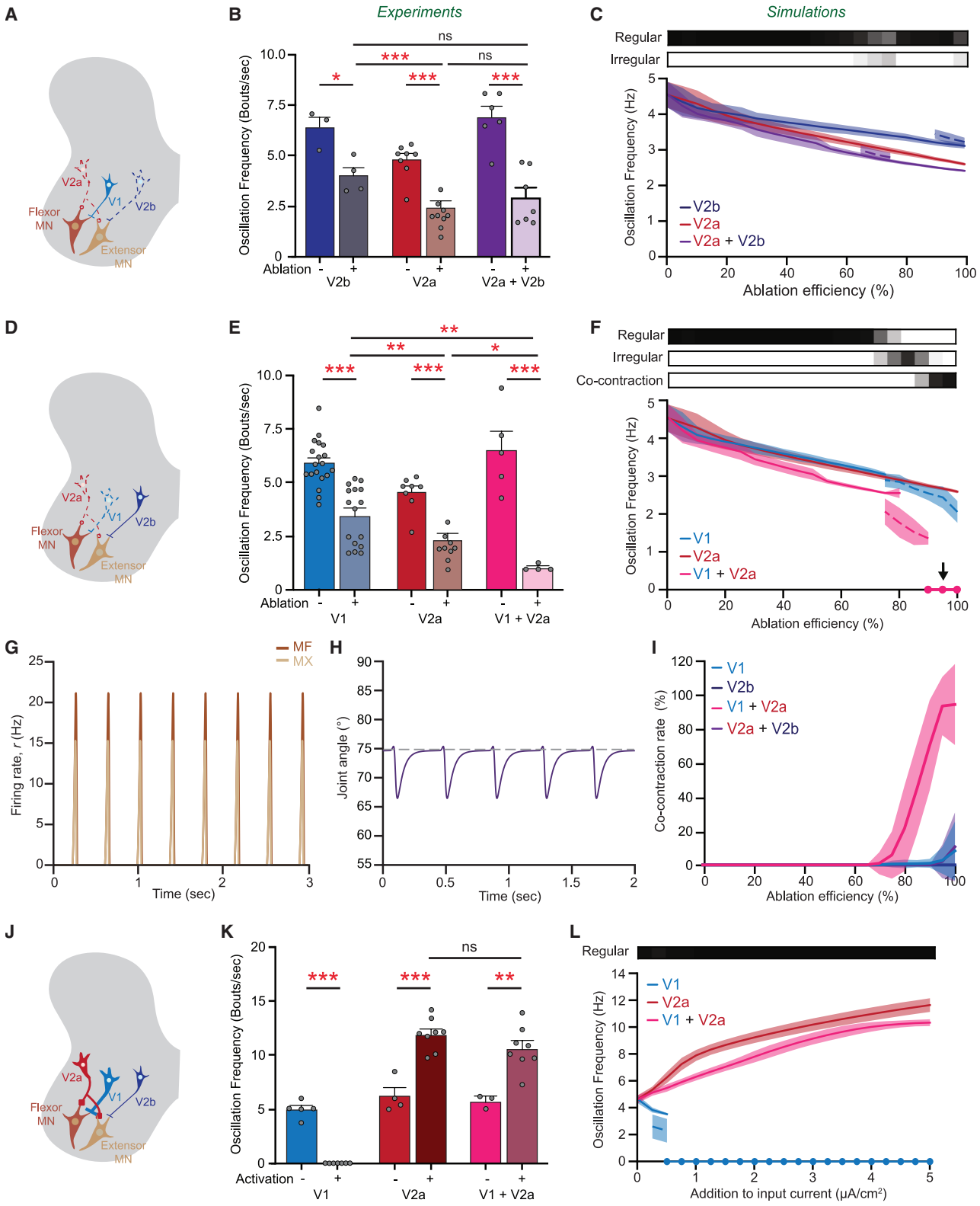

(legend on next page)

equals the effects of the ablation of V2a neurons alone (Figure 6B).

Co-ablation of excitatory V2a and inhibitory V1 neurons (Figures 6D and S6E) strongly disrupted scratch execution (Figures 6E and S6F). Simulating this perturbation also prevents the onset of oscillations (Figures 6F, S6G, and S6H), due to the 100% co-contraction state observed at high-efficiency ablation (Figures 6F, 6G, and 6I). This 100% co-contraction state is not observed when V2a and V2b neurons are co-ablated (Figure 6I), likely because V2b neurons are less abundant than V1 neurons (Figure S4A). Together, these results suggest that inhibitory V1 and excitatory V2a neurons synergistically control the oscillation frequency.

Finally, the co-activation of inhibitory V1 and excitatory V2a neurons (Figures 6J and S6I) caused an increase in the oscillation frequency (Figure 6K), almost to the same extent (not significantly different) as activation of V2a neurons alone, without changes in the number of scratch bouts (Figure S6J). Simulating this perturbation increases the oscillation frequency, to a slightly smaller extent than individual V2a neuron activation (Figures 6L, S6K, and S6L), without inducing irregular bursting or atonia (Figure S6L). Our model also predicts that co-activation of excitatory V2a and inhibitory V2b neurons (Figure S6M) will affect the oscillation frequency to the same extent as individual V2a neuron activation (Figures S6N and S6O).

In summary, we provide experimental and computational evidence that distinct circuit dynamics underlie the cooperation among excitatory (V2a) and inhibitory (V1 and V2b) neurons in controlling the rhythm and phase of motoneuron bursting.

DISCUSSION

We experimentally defined the key contributions that excitatory V2a and inhibitory V1 and V2b neurons make to rhythm generation. To mechanistically explain how excitatory and inhibitory neurons cooperate to drive rhythm, we built and analyzed a neuromechanical model in which inhibitory-coupled flexor and extensor modules drive single-joint oscillations. We showed that individual intra- and inter-module synaptic connections, intrinsic currents, and facilitation mechanisms play a central role in controlling rhythm and phase of motoneuron bursting. Our neuromechanical model not only recapitulates our experimental results but also predicts the role of individual synaptic strengths and the circuit dynamics in the physiological and perturbed execution of the scratch reflex.

Model hypotheses, their effects on neural dynamics and rhythm generation, and predictions

Three conditions are needed for scratch-like oscillations to emerge and be altered in a way that mimics the responses to experimental perturbations: (1) each module should oscillate independently (Figure 4C), (2) intra-module inhibition should be stronger than a critical threshold, whose value increases depending on the strength of the inter-module inhibition (Figure S4H), and (3) facilitation mechanisms should be present in excitatory synapses (Figure S5H).

The E populations act as self-bursting networks, making each module oscillate independently, via an intrinsic mechanism in E neurons that involves two ionic currents, one for depolarization and one, slower, for adaptation (Figures S4D and S4E). Alternative mechanisms of network bursting include tonically firing excitatory neurons with adaptation currents,[48] excitatory neurons recruiting inhibitory neurons via facilitation mechanisms,[35,38] or pure network effects from recurrent excitation and inhibition.[49] Experimentally testing these scenarios requires first identifying the neurons forming individual modules, with rabies-based mapping needed to reveal the identity of module-specific V2a neurons synapsing onto distinct flexor and extensor

Figure 6. Distinct excitatory and inhibitory cooperation dynamics drive scratch rhythm

(A, D, and J) Schematics illustrating the ablation of V2a and V2b neurons (A) and of V1 and V2a neurons (D), and the activation of V1 and V2a neurons (J).

(B) Simultaneous ablation of V2a and V2b neurons reduces the oscillation frequency to the same extent as individual V2a neuron ablation, $^{***}p < 0.0001$ V2a control vs. ablated, $^{*}p = 0.0178$ V2b control vs. ablated, $^{***}p = 0.0002$ V2a and V2b control vs. ablated, $^{***}p = 0.0009$ V2b vs. V2a ablated, $p = 0.1719$ V2b vs. V2a and V2b ablated, $p = 0.1270$ V2a ablated vs. V2a and V2b ablated.

(C) Graph showing the computed oscillation frequency and motoneuron bursting patterns as a function of the ablation efficiency (p) of V2b, V2a, and both V2a and V2b neurons.

(E) Simultaneous ablation of V1 and V2a neurons reduces the oscillation frequency to a greater extent than individual V1 or V2a neuron ablation, $^{***}p < 0.0001$ V1 control vs. ablated, $^{***}p < 0.0001$ V2a control vs. ablated, $^{***}p = 0.0003$ V1 and V2a control vs. ablated, $^{**}p = 0.0057$ V1 vs. V2a ablated, $^{**}p = 0.0027$ V1 vs. V1 and V2a ablated, $^{*}p = 0.0151$ V2a vs. V1 and V2a ablated.

(F) Graph showing the computed oscillation frequency and motoneuron bursting patterns as a function of the ablation efficiency (p) of V1, V2a, and both V1 and V2a neurons. The arrow points to $p = 0.95$ (G and H). For large p values, the circuit settles into a co-contraction state with weak oscillations, here set at zero frequency.

(G and H) Simultaneous ablation of V1 and V2a neurons with high efficiency (>90%) causes a constant co-contraction state, as shown in the simulated time traces of motoneuron firing rate (G) and joint angle (H). This is not considered as an "oscillation" in (F) because the movement does not exceed a 5° extension (STAR Methods).

(I) High-efficiency ablation of only V1 and V2a neurons induces a 100% co-contraction state, as shown by computing the co-contraction rate (STAR Methods) as a function of the ablation efficiency (p).

(K) CNO-driven activation of both V1 and V2a neurons increases frequency, almost to the same extent as individual activation of V2a neurons, $^{***}p < 0.0001$ V1 control vs. activated, $^{***}p < 0.0001$ V2a control vs. activated, $^{**}p = 0.0028$ V1 and V2a control vs. activated, $^{***}p < 0.0001$ V2a vs. V1 activated, $^{***}p < 0.0001$ V1 and V2a vs. V1 activated, $p = 0.1596$ V2a activated vs. V1 and V2a activated.

(L) Graph showing the computed oscillation frequency and motoneuron bursting patterns as a function of the injected current in V1, V2a, and both V1 and V2a neurons.

Experimental data presented as mean ± SEM, individual mice as filled gray circles, SEM as shaded area. Statistical analysis: two-tailed Student's t test. Modeling data presented as mean ± SD of 50 realizations of synaptic conductance parameters, SD as shaded area. Solid and dashed lines in (C), (F), and (L) represent regular and irregular oscillations, respectively. Filled circles indicate atonia in (F) and co-contraction in (L). The bars above the line graphs in (C), (F), and (L) represent the occurrence of each motoneuron bursting pattern as a function of the ablation efficiency (C and F) or the input current (L). See also Figure S6.

Table 1. Model parameters for the neuronal model

Parameter definition	Symbol	Value
Input current	$I_{inp}^{E\alpha}$	0.6 μA/cm^2
	$I_{inp}^{I\alpha}$	0.3 μA/cm^2
	$I_{inp}^{M\alpha}$	0
Fraction of V1 neurons in I populations	κ^{IX}	0.82
	κ^{IF}	0.45
Synaptic time constant	$\tau_s^{E\alpha}$	4.0 ms
	$\tau_s^{I\alpha}$, $\tau_s^{M\alpha}$	5.4 ms
Facilitation time constant	$\tau_u^{E\alpha}$	250 ms
Adaptation current time constant	$\tau_a^{E\alpha}$	167 ms
	$\tau_a^{I\alpha}$	63 ms
	$\tau_a^{M\alpha}$	500 ms
Adaptation current strength	$J_a^{E\alpha}$, $J_a^{M\alpha}$	140 ms × μA/cm^2
	$J_a^{I\alpha}$	180 ms × μA/cm^2
Depolarization current time constant	$\tau_d^{E\alpha}$	1.9 ms
Depolarization current strength	$J_d^{E\alpha}$	110 ms × μA/cm^2
Slope of f-I curve	β_r	0.011 cm^2/(ms x μA)
Utilization of synaptic efficacy	$U^{E\alpha}$	0.03
	$u^{I\alpha}$, $u^{M\alpha}$	0.4
Available synaptic resource	$x^{E\alpha}$	0.92
	$x^{I\alpha}$, $x^{M\alpha}$	0.48
Synaptic coupling coefficients	J_{intra}^{IE}	52 μA/cm^2
	J_{intra}^{ME}	195 μA/cm^2
	J_{inter}^{EE}	6.5 μA/cm^2
	J_{intra}^{EI}	66 μA/cm^2
	J_{inter}^{EI}	77 μA/cm^2
	J_{inter}^{II}	55 μA/cm^2
	J_{inter}^{MI}	330 μA/cm^2

When an index α is written, the parameter value is valid for α = F, X. Synaptic coupling coefficients that are not listed in this table are 0.

motoneuron pools. Intersectional genetics and viral approaches to reconstruct the physiological connectivity of module-specific V2a neurons will allow defining the intrinsic and network properties leading to self-bursting, as well as identifying the cellular components of each module.

In CPG models lacking intra-module inhibition,[33,44,50] blocking inhibition accelerates rhythm or, under restricted parameter regimens, leaves it almost unaffected.[44] The discrepancies between these models and our experimental results prompted us to evaluate the contribution of individual inhibitory synapses to rhythmogenesis. Weakening the intra- and inter-module I-to-E inhibition reduces and increases the oscillation frequency, respectively (Figures 4F and S4G). Thus, to decrease frequency, reductions in the overall inhibition or excitation should weaken intra- more than inter-module inhibition (Figures S4H and S5B). The predicted differences in synaptic strength of the distinct inhibitory synapses remain to be experimentally validated. The intra- and inter-module inhibitory synapses might originate from the same neurons or from specialized subsets within the inhibitory populations. For instance, recent work shows that the Pou6f2-subset of V1 neurons is required for their rhythmogenic function,[11] suggesting that this subset might be key in mediating intra-module inhibition.

Our model hypothesizes the presence of facilitation mechanisms in E neurons. Activation of V2a neurons increases the firing rate and, via facilitation (Figure S5H), increases the effective intra-module excitation that accelerates rhythm (Figure S4F). An alternative solution is that the activation-driven increase in bursting is due to intrinsic neuronal properties, as shown in other models,[34] or is due to a combination of intrinsic properties and E-to-E synaptic connections.[48] Whether the increase in oscillation frequency is due to facilitation, intrinsic mechanisms, or a combination of both remains to be assessed. Finally, the increase in frequency causes a reduction in amplitude, both in experimental (Figures S1D and S1E) and computational (Figures 4D, S4E, and S4F) observations, begging the question of how facilitation promotes frequency over amplitude.

Finally, more experiments are required to validate our model predictions on (1) the effects of activation of V2b neurons individually (Figure 5L) and with V2a neurons (Figures S6M–S6O), (2) the perturbation-induced phase differences (Figures 5 and 6), and (3) the frequency changes as a function of the perturbation efficiency (Figures 5 and 6).

Comparison with cell-type-agnostic models for rhythmic scratching

In our rate model, rhythm is driven by a self-bursting population of excitatory neurons (E), while inhibitory neurons (I) have a dual function, they control the bursting frequency via the intra- and inter-module I-to-E inhibition (Figures 4F and S4G) and the phase of flexor and extensor motoneuron bursting via inter-module I-to-E and I-to-I inhibitory connections (Figure 4A). These findings address important gaps in current models by providing mechanistic explanations on the cooperation dynamics of genetically identified excitatory and inhibitory neurons and on the contribution of distinct inhibitory synapses as a function of their relative strengths.

Previous work in turtles suggests that the scratch rhythm is generated by a balanced E-I neural network,[51] with neural activity resembling "rotational dynamics" at the population level.[49] In this model that exhibits the hallmarks of a fluctuation-driven regimen, synaptic coupling[49,52] is strong, random, and sparse.[53] Population frequency is modulated by adjusting the gain of "speed" or "break" subsets that are a mix of excitatory and inhibitory neurons. However, in contrast to ours, the rotational dynamics model does not include genetically identified neuron populations, and its robustness in recapitulating experimental perturbations remains to be validated. A future challenge is to convert our rate model into a spiking, strongly coupled neural model, like the rotational dynamic model, preserving the network architecture and the strong intra-module inhibition. This will enable us to assess how the irregular temporal dynamics of E and I input, in physiological and perturbed states, determine the frequency and the phase difference of motoneuron bursting.

A more recent model includes two sparse, randomly connected networks coupled via mutual inhibition[54] in which excitatory neurons possess a slow current that drives bursting only in a subset of neurons.[54] The intra-module inhibition widens the range of firing phases within each neuronal population,[54]

Table 2. Model parameters for the biomechanical model

Parameter definition	Symbol	Value
Segment mass	M	0.4 g
Segment length	L_d	1 cm
Distance between rotation axis and segment center of mass	d	0.1 cm
Distance between muscle contact point and insertion point	a	1.8 cm
Distance between rotation axis and muscle contact point	b	0.1 cm
Joint viscosity	B	3×10^9 dyn $\times$ cm $\times$ s
Optimal muscle length	L_0	0.473 cm
Maximum muscle length/optimal muscle length	α_L	1.1
Minimum joint angle	θ_{min}	40°
Maximum joint angle	θ_{max}	110°
Parameters determine rotation range	T_A^S	1000 dyn
	σ^S	0.01 rad
Muscle activation time constants	τ_1, τ_2	0.01 s
Maximum muscle force	F_0	2.13×10^5 dyn
Normalization constant for motoneuron firing rate	r_0	54 Hz
Passive force	c_1	128
	k_1	0.046
	L_{r1}	1.17
Length-dependent muscle activation	α_f	0.56
	n_{f0}	2.1
	n_{f1}	3.3
Active force-length relationship	β_{FL}	1.55
	ω	0.75
	ρ	2.12

making the firing phase distribution closer, but not equal, to what is predicted by the rotational dynamics model.[49] Increases in intra-module inhibition cause firing irregularities, a main hallmark of fluctuation-driven regimens, as observed in models of two coupled inhibitory populations.[33] Whether in this model, as predicted by ours, inter-module inhibition exerts opposite effects on rhythmogenesis remains to be assessed.

Cooperation of excitatory and inhibitory neurons in flexor and extensor coordination

While individual ablation of V1 and V2b neurons results in hyper-flexion and hyper-extension, respectively,[15] ablation of V1 and V2b neurons together with V2a neurons revealed more complex dynamics. Co-ablation of V2a and V2b neurons rescues the leg hyper-extension phenotype caused by individual V2b neuron ablation,[15,31] whereas co-ablation of V1 and V2a neurons severely worsens the flexor and extensor impairments caused by ablation of V1 neurons alone (Figures 6F–6I). This correlates with a 100% co-contraction state observed following co-ablation of V1 and V2a neurons, but not of V2a and V2b neurons (Figure 6I). This differential effect might simply be due to V1 neurons being more numerous (Figure S4A) or to distinct intrinsic properties and/or connectivity of the two inhibitory populations.

Evolutionary divergence or convergence of spinal circuits for fast rhythms

In behaving mice, perturbations of excitatory Chx10-V2a neurons affect the scratch (Figure 2) but not the locomotor rhythm,[6] likely due to the compensation exerted by Shox2-V2a neurons during walking.[7] As scratching is ~2.3 times faster than walking,[55] an intriguing hypothesis is that scratch and locomotion, similar to fast and slow swimming in zebrafish,[4,56] require two distinct subsets of V2a neurons: Shox2-V2a neurons for slow and Chx10-V2a neurons for faster rhythms. V1 neurons contribute to fast swimming in zebrafish by inhibiting slow motoneurons,[12] and in mouse to *in vitro* locomotor,[10,11] and *in vivo* scratch rhythm (Figures 3B–3D). Together these findings might suggest that inhibitory V1 and excitatory V2a might represent a conserved microcircuit between zebrafish and mice to drive slow and fast rhythms.

V2b neurons are a conundrum. Ablating V2b neurons increases tail oscillation frequency in zebrafish[14] and reduces limb oscillation frequency in mice (Figures 3H, 3I, and S3I), raising the question on whether V2b neurons have acquired a specialized function in limbed animals.

In conclusion, we theorize an evolutionary conserved strategy, with fast oscillations of a single joint in limbed animals driven by similar dynamics as undulatory movements in aquatic animals.

Limitations of the study

Scratching is driven by CPG neurons in the absence of sensory feedback.[57–60] Most of the rhythmically active neurons reside in lamina VII, with population activity resembling rotational dynamics,[49] but with individual neurons tuned to specific phases.[58,61] For example, Ia neurons, a subset of both V1 and V2b neuronal populations, fire in phase with agonist motoneurons.[61,62] Current limitations in recording neural activity *in vivo* precluded us from determining the firing patterns of CPG neurons during scratching, and the strength of the network synaptic coupling. Thus, to define the neuronal mechanisms underlying scratch rhythmogenesis, we used a mean-driven network model.[63] Should *in vivo* recordings show strong variability of firing patterns or sparse network connectivity, as observed in turtles,[64,65] our model will require updating to a "fluctuation-driven regimen" or "strong coupling scenario."

In summary, future *in vivo* recording experiments are needed to determine the timing and phase of firing of genetically identified neurons onto motoneurons. Defining the temporal pattern of activity of V1, V2a, and V2b neurons will enable time-locking the optogenetic activation/inactivation of each neuron type to its active phase, providing a better time resolution for interpreting the effects of perturbations of neuronal activity.

RESOURCE AVAILABILITY

Lead contact

Information and requests for resources and reagents should be directed to and will be fulfilled by the lead contact, Graziana Gatto (graziana.gatto@uk-koeln.de).

Materials availability

All reagents and mouse lines will be shared upon request within the limits of the respective material transfer agreements.

Data and code availability

- Original data reported in this paper are available from the lead contact on request.
- All original code is publicly available on GitHub (https://doi.org/10.5281/zenodo.15328238).
- Any additional information required to re-analyze the data reported in this paper is available from the lead contact upon request.

ACKNOWLEDGMENTS

We thank members of the NIHU19-SCC, Quinn Silverman, and Marianna Tolve for discussions and feedback on the manuscript. This work was funded by the National Institutes of Health Brain Initiative (NIH-U19NS112959 to M.G., D.G., G.G., T.S., and E.A.; NIH-R01NS111643 to M.G.; NIH-RF1NS128898 to E.A.; and NINDS-F32NS126231 to A.N.), the German Research Foundation (CRC1451, Project ID 431549029-A09 to G.G.), and the Israel Science Foundation (1511/24 to D.G.). G.G. is part of the iBehave network.

AUTHOR CONTRIBUTIONS

Conceptualization: E.A., M.G., T.S., D.G., and G.G.; methodology: M.Y., A.N., S.C.M., T.S., D.G., and G.G.; investigation: M.Y., A.N., D.G., and G.G.; writing original draft: M.Y., D.G., and G.G.; review & editing: M.Y., A.N., E.A., M.G., T.S., D.G., and G.G.; funding acquisition, E.A., M.G., T.S., D.G., and G.G.; supervision: E.A., M.G., T.S., D.G., and G.G.

DECLARATION OF INTERESTS

The authors declare no competing interests.

STAR★METHODS

Detailed methods are provided in the online version of this paper and include the following:

- KEY RESOURCES TABLE
- EXPERIMENTAL MODEL AND STUDY PARTICIPANT DETAILS
- METHOD DETAILS
  - Neuronal ablation
  - Drug administration
  - Chloroquine-induced scratching
  - Neuronal activity manipulations and behavioral testing
  - cFos expression following chloroquine-induced scratching
  - Biophysical neuronal rate model
  - Biomechanical model
  - Calculation of oscillation frequency and identification of dynamics categories
  - Simulations and visualization
- QUANTIFICATION AND STATISTICAL ANALYSIS

SUPPLEMENTAL INFORMATION

Supplemental information can be found online at https://doi.org/10.1016/j.celrep.2025.115845.

Received: January 24, 2025
Revised: April 1, 2025
Accepted: May 23, 2025
Published: June 17, 2025

REFERENCES

1. Goulding, M. (2009). Circuits controlling vertebrate locomotion: moving in a new direction. Nat. Rev. Neurosci. *10*, 507–518.
2. Kiehn, O. (2016). Decoding the organization of spinal circuits that control locomotion. Nat. Rev. Neurosci. *17*, 224–238.
3. Dougherty, K.J., and Ha, N.T. (2019). The rhythm section: an update on spinal interneurons setting the beat for mammalian locomotion. Curr. Opin. Physiol. *8*, 84–93.
4. Ampatzis, K., Song, J., Ausborn, J., and El Manira, A. (2014). Separate Microcircuit Modules of Distinct V2a Interneurons and Motoneurons Control the Speed of Locomotion. Neuron *83*, 934–943.
5. Crone, S.A., Quinlan, K.A., Zagoraiou, L., Droho, S., Restrepo, C.E., Lundfald, L., Endo, T., Setlak, J., Jessell, T.M., Kiehn, O., and Sharma, K. (2008). Genetic ablation of V2a ipsilateral interneurons disrupts left-right locomotor coordination in mammalian spinal cord. Neuron *60*, 70–83.
6. Crone, S.A., Zhong, G., Harris-Warrick, R., and Sharma, K. (2009). In mice lacking V2a interneurons, gait depends on speed of locomotion. J. Neurosci. *29*, 7098–7109.
7. Dougherty, K.J., Zagoraiou, L., Satoh, D., Rozani, I., Doobar, S., Arber, S., Jessell, T.M., and Kiehn, O. (2013). Locomotor rhythm generation linked to the output of spinal shox2 excitatory interneurons. Neuron *80*, 920–933.
8. Zhang, Y., Narayan, S., Geiman, E., Lanuza, G.M., Velasquez, T., Shanks, B., Akay, T., Dyck, J., Pearson, K., Gosgnach, S., et al. (2008). V3 spinal neurons establish a robust and balanced locomotor rhythm during walking. Neuron *60*, 84–96.
9. Caldeira, V., Dougherty, K.J., Borgius, L., and Kiehn, O. (2017). Spinal Hb9::Cre-derived excitatory interneurons contribute to rhythm generation in the mouse. Sci. Rep. *7*, 41369.
10. Gosgnach, S., Lanuza, G.M., Butt, S.J.B., Saueressig, H., Zhang, Y., Velasquez, T., Riethmacher, D., Callaway, E.M., Kiehn, O., and Goulding, M. (2006). V1 spinal neurons regulate the speed of vertebrate locomotor outputs. Nature *440*, 215–219.
11. Trevisan, A.J., Han, K., Chapman, P., Kulkarni, A.S., Hinton, J.M., Ramirez, C., Klein, I., Gatto, G., Gabitto, M.I., Menon, V., and Bikoff, J.B. (2024). The transcriptomic landscape of spinal V1 interneurons reveals a role for En1 in specific elements of motor output. Preprint at bioRxiv. https://doi.org/10.1101/2024.09.18.613279.
12. Kimura, Y., and Higashijima, S.I. (2019). Regulation of locomotor speed and selection of active sets of neurons by V1 neurons. Nat. Commun. *10*, 2268.
13. Vijatovic, D., Toma, F.A., Harrington, Z.P.M., Sommer, C., Hauschild, R., Trevisan, A.J., Chapman, P., Julseth, M.J., Brenner-Morton, S., Gabitto, M.I., et al. (2024). Spinal neuron diversity scales exponentially with swim-to-limb transformation during frog metamorphosis. Preprint at bioRxiv. https://doi.org/10.1101/2024.09.20.614050.
14. Callahan, R.A., Roberts, R., Sengupta, M., Kimura, Y., Higashijima, S.I., and Bagnall, M.W. (2019). Spinal V2b neurons reveal a role for ipsilateral inhibition in speed control. eLife *8*, e47837.
15. Britz, O., Zhang, J., Grossmann, K.S., Dyck, J., Kim, J.C., Dymecki, S., Gosgnach, S., and Goulding, M. (2015). A genetically defined asymmetry underlies the inhibitory control of flexor-extensor locomotor movements. eLife *4*, e04718.
16. Perkel, D.H., and Mulloney, B. (1974). Motor Pattern Production in Reciprocally Inhibitory Neurons Exhibiting Postinhibitory Rebound. Science *185*, 181–183.
17. Friesen, W.O., and Stent, G.S. (1977). Generation of a locomotory rhythm by a neural network with recurrent cyclic inhibition. Biol. Cybern. *28*, 27–40.
18. McCrea, D.A., and Rybak, I.A. (2008). Organization of mammalian locomotor rhythm and pattern generation. Brain Res. Rev. *57*, 134–146.
19. Brown, T.G. (1911). The Intrinsic Factors in the Act of Progression in the Mammal. Proc. R. Soc. London B Biol. Sci. *84*, 308–319.

20. Brown, T.G. (1914). On the nature of the fundamental activity of the nervous centres; together with an analysis of the conditioning of rhythmic activity in progression, and a theory of the evolution of function in the nervous system. J. Physiol. *48*, 18–46.

21. Bellardita, C., and Kiehn, O. (2015). Phenotypic characterization of speed-associated gait changes in mice reveals modular organization of locomotor networks. Curr. Biol. *25*, 1426–1436.

22. Talpalar, A.E., Bouvier, J., Borgius, L., Fortin, G., Pierani, A., and Kiehn, O. (2013). Dual-mode operation of neuronal networks involved in left–right alternation. Nature *500*, 85–88.

23. Zhang, H., Shevtsova, N.A., Deska-Gauthier, D., Mackay, C., Dougherty, K.J., Danner, S.M., Zhang, Y., and Rybak, I.A. (2022). The role of V3 neurons in speeddependent interlimb coordination during locomotion in mice. eLife *11*, e73424.

24. Pinto, C.M.A., and Golubitsky, M. (2006). Central pattern generators for bipedal locomotion. J. Math. Biol. *53*, 474–489.

25. Sherrington, C.S. (1910). Notes on the scratch-reflex of the cat. Q. J. Exp. Physiol. *3*, 213–220.

26. Frigon, A. (2012). Central pattern generators of the mammalian spinal cord. Neuroscientist *18*, 56–69.

27. Hunt, S.P., Pini, A., and Evan, G. (1987). Induction of c-fos-like protein in spinal cord neurons following sensory stimulation. Nature *328*, 632–634.

28. Bourane, S., Duan, B., Koch, S.C., Dalet, A., Britz, O., Garcia-Campmany, L., Kim, E., Cheng, L., Ghosh, A., Ma, Q., and Goulding, M. (2015). Gate control of mechanical itch by a subpopulation of spinal cord interneurons. Science *350*, 550–554.

29. Sciolino, N.R., Plummer, N.W., Chen, Y.W., Alexander, G.M., Robertson, S.D., Dudek, S.M., McElligott, Z.A., and Jensen, P. (2016). Recombinase-Dependent Mouse Lines for Chemogenetic Activation of Genetically Defined Cell Types. Cell Rep. *15*, 2563–2573.

30. Zhang, J., Lanuza, G.M., Britz, O., Wang, Z., Siembab, V.C., Zhang, Y., Velasquez, T., Alvarez, F.J., Frank, E., and Goulding, M. (2014). V1 and v2b interneurons secure the alternating flexor-extensor motor activity mice require for limbed locomotion. Neuron *82*, 138–150.

31. Hayashi, M., Gullo, M., Senturk, G., Costanzo, S.D., Nagasaki, S.C., Kageyama, R., Imayoshi, I., Goulding, M., Pfaff, S.L., and Gatto, G. (2023). A spinal synergy of excitatory and inhibitory neurons coordinates ipsilateral body movements. eLife *12*, RP89362.

32. Shriki, O., Hansel, D., and Sompolinsky, H. (2003). Rate models for conductance-based cortical neuronal networks. Neural Comput. *15*, 1809–1841.

33. Golomb, D., Moore, J.D., Fassihi, A., Takatoh, J., Prevosto, V., Wang, F., and Kleinfeld, D. (2022). Theory of hierarchically organized neuronal oscillator dynamics that mediate rodent rhythmic whisking. Neuron *110*, 3833–3851.

34. Golomb, D., Shedmi, A., Curtu, R., and Ermentrout, G.B. (2006). Persistent synchronized bursting activity in cortical tissues with low magnesium concentration: a modeling study. J. Neurophysiol. *95*, 1049–1067.

35. Hayut, I., Fanselow, E.E., Connors, B.W., and Golomb, D. (2011). LTS and FS inhibitory interneurons, short-term synaptic plasticity, and cortical circuit dynamics. PLoS Comput. Biol. *7*, e1002248.

36. Reid, B., Slater, C.R., and Bewick, G.S. (1999). Synaptic vesicle dynamics in rat fast and slow motor nerve terminals. J. Neurosci. *19*, 2511–2521.

37. Jackman, S.L., and Regehr, W.G. (2017). The Mechanisms and Functions of Synaptic Facilitation. Neuron *94*, 447–464.

38. Melamed, O., Barak, O., Silberberg, G., Markram, H., and Tsodyks, M. (2008). Slow oscillations in neural networks with facilitating synapses. J. Comput. Neurosci. *25*, 308–316.

39. Dougherty, K.J., and Kiehn, O. (2010). Firing and cellular properties of V2a interneurons in the rodent spinal cord. J. Neurosci. *30*, 24–37.

40. Azim, E., Jiang, J., Alstermark, B., and Jessell, T.M. (2014). Skilled reaching relies on a V2a propriospinal internal copy circuit. Nature *508*, 357–363.

41. Hayashi, M., Hinckley, C.A., Driscoll, S.P., Moore, N.J., Levine, A.J., Hilde, K.L., Sharma, K., and Pfaff, S.L. (2018). Graded Arrays of Spinal and Supraspinal V2a Interneuron Subtypes Underlie Forelimb and Hindlimb Motor Control. Neuron *97*, 869–884.

42. Tsianos, G.A., and Loeb, G.E. (2017). Muscle and Limb Mechanics. Compr. Physiol. *7*, 429–462.

43. Brown, I.E., Cheng, E.J., and Loeb, G.E. (1999). Measured and modeled properties of mammalian skeletal muscle. II. The effects of stimulus frequency on force-length and force-velocity relationships. J. Muscle Res. Cell Motil. *20*, 627–643.

44. Ausborn, J., Snyder, A.C., Shevtsova, N.A., Rybak, I.A., and Rubin, J.E. (2018). State-dependent rhythmogenesis and frequency control in a half-center locomotor CPG. J. Neurophysiol. *119*, 96–117.

45. Rinzel, J., and Ermentrout, G.B. (1998). Analysis of neural excitability and oscillations. In Methods in Neuronal Modeling, Second Edition, C. Koch and I. Segev, eds. (MIT Press), pp. 251–292.

46. Bertram, R., Butte, M.J., Kiemel, T., and Sherman, A. (1995). Topological and phenomenological classification of bursting oscillations. Bull. Math. Biol. *57*, 413–439.

47. Schuster, H.G., and Just, W. (2005). Deterministic Chaos: An Introduction, Fourth Edition (Wiley-VCH), pp. 1–287.

48. Van Vreeswijk, C., and Hansel, D. (2001). Patterns of synchrony in neural networks with spike adaptation. Neural Comput. *13*, 959–992.

49. Lindén, H., Petersen, P.C., Vestergaard, M., and Berg, R.W. (2022). Movement is governed by rotational neural dynamics in spinal motor networks. Nature *610*, 526–531.

50. Soloduchin, S., and Shamir, M. (2018). Rhythmogenesis evolves as a consequence of long-term plasticity of inhibitory synapses. Sci. Rep. *8*, 13050.

51. Berg, R.W., Alaburda, A., and Hounsgaard, J. (2007). Balanced inhibition and excitation drive spike activity in spinal half-centers. Science *315*, 390–393.

52. Lindén, H., and Berg, R.W. (2021). Why Firing Rate Distributions Are Important for Understanding Spinal Central Pattern Generators. Front. Hum. Neurosci. *15*, 719388.

53. Berg, R.W. (2017). Neuronal population activity in spinal motor circuits: Greater than the sum of its parts. Front. Neural Circuits *11*, 294694.

54. Strohmer, B., Najarro, E., Ausborn, J., Berg, R.W., and Tolu, S. (2024). Sparse Firing in a Hybrid Central Pattern Generator for Spinal Motor Circuits. Neural Comput. *36*, 759–780.

55. Frigon, A., and Gossard, J.P. (2010). Evidence for specialized rhythm-generating mechanisms in the adult mammalian spinal cord. J. Neurosci. *30*, 7061–7071.

56. Song, J., Pallucchi, I., Ausborn, J., Ampatzis, K., Bertuzzi, M., Fontanel, P., Picton, L.D., and El Manira, A. (2020). Multiple Rhythm-Generating Circuits Act in Tandem with Pacemaker Properties to Control the Start and Speed of Locomotion. Neuron *105*, 1048–1061.

57. Jankowska, E. (1959). Instrumental scratch reflex of the deafferented limb in cats and rats. Acta Biol. Exp. *19*, 233–247.

58. Berkinblit, M.B., Deliagina, T.G., Feldman, A.G., Gelfand, I.M., and Orlovsky, G.N. (1978). Generation of scratching. I. Activity of spinal interneurons during scratching. J. Neurophysiol. *41*, 1040–1057.

59. Berkinblit, M.B., Deliagina, T.G., Feldman, A.G., Gelfand, I.M., and Orlovsky, G.N. (1978). Generation of scratching. II. Nonregular regimes of generation. J. Neurophysiol. *41*, 1058–1069.

60. Deliagina, T.G., Orlovsky, G.N., and Pavlova, G.A. (1983). The Capacity for generation of rhythmic oscillations is distributed in the lumbosacral spinal cord of the cat. Exp. Brain Res. *531*, 81–90.

61. Baev, K.V., Degtiarenko, A.M., Zavadskaia, T.V., and Kostiuk, P.G. (1981). Activity of interneurons of the lumbosacral division of the spinal cord during fictive scratching. Neirofiziologiia *13*, 58–66.

62. Deliagina, T.G., and Orlovsky, G.N. (1980). Activity of Ia inhibitory interneurons during fictitious scratch reflex in the cat. Brain Res. *193*, 439–447.

63. Pehlevan, C., and Sompolinsky, H. (2014). Selectivity and sparseness in randomly connected balanced networks. PLoS One *9*, e89992.

64. Petersen, P.C., and Berg, R.W. (2016). Lognormal firing rate distribution reveals prominent fluctuation-driven regime in spinal motor networks. eLife *5*, e18805.

65. Radosevic, M., Willumsen, A., Petersen, P.C., Lindén, H., Vestergaard, M., and Berg, R.W. (2019). Decoupling of timescales reveals sparse convergent CPG network in the adult spinal cord. Nat. Commun. *10*, 2937.

66. Bourane, S., Grossmann, K.S., Britz, O., Dalet, A., Del Barrio, M.G., Stam, F.J., Garcia-Campmany, L., Koch, S., and Goulding, M. (2015). Identification of a spinal circuit for light touch and fine motor control. Cell *160*, 503–515.

67. Sapir, T., Geiman, E.J., Wang, Z., Velasquez, T., Mitsui, S., Yoshihara, Y., Frank, E., Alvarez, F.J., and Goulding, M. (2004). Pax6 and engrailed 1 regulate two distinct aspects of renshaw cell development. J. Neurosci. *24*, 1255–1264.

68. Duan, B., Cheng, L., Bourane, S., Britz, O., Padilla, C., Garcia-campmany, L., Krashes, M., Knowlton, W., Velasquez, T., Ren, X., et al. (2014). Identification of Spinal Circuits Transmitting and Gating Mechanical Pain. Cell *159*, 1417–1432.

69. Sengupta, M., and Bagnall, M.W. (2023). Spinal Interneurons: Diversity and Connectivity in Motor Control. Annu. Rev. Neurosci. *46*, 79–99.

70. Deliagina, T.G., Feldman, A.G., Gelfand, I.M., and Orlovsky, G.N. (1975). On the role of central program and afferent inflow in the control of scratching movements in the cat. Brain Res. *100*, 297–313.

71. Tsodyks, M., Pawelzik, K., and Markram, H. (1998). Neural networks with dynamic synapses. Neural Comput. *10*, 821–835.

72. Silberberg, G., and Markram, H. (2007). Disynaptic inhibition between neocortical pyramidal cells mediated by Martinotti cells. Neuron *53*, 735–746.

73. Bikoff, J.B., Gabitto, M.I., Rivard, A.F., Drobac, E., Machado, T.A., Miri, A., Brenner-Morton, S., Famojure, E., Diaz, C., Alvarez, F.J., et al. (2016). Spinal Inhibitory Interneuron Diversity Delineates Variant Motor Microcircuits. Cell *165*, 207–219.

74. Husch, A., Dietz, S.B., Hong, D.N., and Harris-Warrick, R.M. (2015). Adult spinal V2a interneurons show increased excitability and serotonin-dependent bistability. J. Neurophysiol. *113*, 1124–1134.

75. Charles, J.P., Cappellari, O., Spence, A.J., Wells, D.J., and Hutchinson, J.R. (2016). Muscle moment arms and sensitivity analysis of a mouse hindlimb musculoskeletal model. J. Anat. *229*, 514–535.

76. Song, D., Raphael, G., Lan, N., and Loeb, G.E. (2008). Computationally efficient models of neuromuscular recruitment and mechanics. J. Neural. Eng. *5*, 175–184.

77. Meyer, G., and Lieber, R.L. (2018). Muscle fibers bear a larger fraction of passive muscle tension in frogs compared with mice. J. Exp. Biol. *221*, jeb182089.

78. Smith, L.R., Lee, K.S., Ward, S.R., Chambers, H.G., and Lieber, R.L. (2011). Hamstring contractures in children with spastic cerebral palsy result from a stiffer extracellular matrix and increased in vivo sarcomere length. J. Physiol. *589*, 2625–2639.

79. Todorov, E. (2005). Stochastic optimal control and estimation methods adapted to the noise characteristics of the sensorimotor system. Neural Comput. *17*, 1084–1108.

80. Baldissera, F., Cavallari, P., and Cerri, G. (1998). Motoneuronal precompensation for the low-pass filter characteristics of muscle. A quantitative appraisal in cat muscle units. J. Physiol. *511*, 611–627.

81. Martínez-Silva, M. de L., Imhoff-Manuel, R.D., Sharma, A., Heckman, C.J., Shneider, N.A., Roselli, F., Zytnicki, D., and Manuel, M. (2018). Hypoexcitability precedes denervation in the large fast-contracting motor units in two unrelated mouse models of ALS. eLife *7*, e30955.

82. Rassier, D.E., MacIntosh, B.R., and Herzog, W. (1999). Length dependence of active force production in skeletal muscle. J. Appl. Physiol. *86*, 1445–1457.

83. Herzog, W., Kamal, S., and Clarke, H.D. (1992). Myofilament lengths of cat skeletal muscle: theoretical considerations and functional implications. J. Biomech. *25*, 945–948.

STAR★METHODS

KEY RESOURCES TABLE

REAGENT or RESOURCE	SOURCE	IDENTIFIER
Antibodies		
Rabbit dsRed (1:1000)	Takara Bio	Cat# 632392; RRID:AB_2801258
Rabbit c-Fos (1:500)	Santa Cruz	Cat# sc-52; RRID:AB_2106783
Rabbit c-Fos (1:1000)	Cell Signaling Technology	Cat#2250; RRID:AB_2247211
Chemicals, peptides, and recombinant proteins		
Chloroquine	Sigma	C6628
Clozapine N-oxide (CNO)	Sigma	C0832
Diphtheria Toxin (DTx)	List Biological Lab	#150
Saline Solution	APP Pharmaceuticals	NDC63323-186-10
Experimental models: Organisms/strains		
Mouse: *Chx10*^{Cre}	Azim et al. 2014[40]	
Mouse: *hCdx2::FlpO*	Bourane et al. 2015b[66]	
Mouse: *En1*^{Cre}	Sapir at al. 2004[67]	
Mouse: *Hes2*^{iCre}	Hayashi et al. 2023[31]	
Mouse: *R26*$^{ds\text{-}hM3Dq}$	Jackson Laboratory	RRID:IMSR_JAX:026942
Mouse: *R26*$^{ds\text{-}hM4Di}$	Bourane et al. 2015a[28]	
Mouse: *R26*$^{Ai14\text{-}Td\text{-}Tomato}$	Jackson Laboratory	RRID:IMSR_JAX:007914
Mouse: *R26*$^{Ai65\text{-}ds\text{-}Td\text{-}Tomato}$	Jackson Laboratory	RRID:IMSR_JAX:021875
Mouse: *Tau*$^{ds\text{-}DTR}$	Duan et al. 2014[68]	
Software and algorithms		
Neuromechanical model	This publication	https://doi.org/10.5281/zenodo.15328238
Adobe Creative Cloud	Adobe	www.adobe.com
Excel-Office 2018	Microsoft	www.microsoft.com
ImageJ		ImageJ.nih.gov/ij
Prism	GraphPad	www.graphpad.com
R	The R project	r-project.org
Python		https://www.python.org
SIMI Motion	SIMI	http://www.simi.com/en/

EXPERIMENTAL MODEL AND STUDY PARTICIPANT DETAILS

Mice were maintained following the protocols for animal experiments approved by the IACUC of the Salk Institute for Biological Studies according to NIH guidelines for animal experimentation, and by the local health authority in North Rhein Westphalia (LAVE). All mice used in experiments were housed in a regular light cycle room with food and water available *ad libitum*. Mouse lines used to target spinal neurons: *hCdx2::FlpO;En1*^{Cre} (V1), *hCdx2::FlpO;Chx10*^{Cre} (V2a), *VGAT*^{FlpO}*;Hes2*^{iCre} (V2b), *hCdx2::FlpO;En1*^{Cre}*;Chx10*^{Cre} (V1 and V2a) and *hCdx2::FlpO;Hes2i*^{Cre} (V2a and V2b). Mouse lines used for labeling or perturbing neurons: *R26*$^{ds\text{-}hM3Dq}$ (neuronal activation), *R26*$^{ds\text{-}hM4Di}$ (neuronal silencing), *R26*$^{Ai14\text{-}Td\text{-}Tomato}$ and *R26*$^{Ai65\text{-}ds\text{-}Td\text{-}Tomato}$ (fluorescent labeling), *Tau*$^{ds\text{-}DTR}$ (neuronal ablation). Transgenic mouse strains were used and maintained on a mixed genetic background (C57BL6/J, 129S1/Sv and CD1). 6- to 10-week-old mice of both sexes were used for behavioral experiments. Analysis of the behavioral data showed similar responses in male and female mice.

METHOD DETAILS

Neuronal ablation

Mice carrying the *En1*^{Cre}*;hCdx2::FlpO, Chx10*^{Cre}*;hCdx2::FlpO, Hes2*^{iCre}*;hCdx2::FlpO, En1*^{Cre}*;Chx10*^{Cre}*;hCdx2::FlpO* alleles in addition to the effector allele *Tau*$^{ds\text{-}DTR}$ received i.p. injections of diphtheria toxin (DTx, 50 ng/g of weight; List Biological Laboratories)

at P28 and P31. *Hes2*^{iCre};*VGAT*^{FlpO};*Tau*$^{ds\text{-}DTR}$ mice and the littermate controls *Hes2*^{iCre};*Tau*$^{ds\text{-}DTR}$ received intrathecal injections of diphtheria toxin (DTx, 10 ng; List Biological Laboratories) at P28, P30 and P32. *FlpO* negative mice injected with DTx were used as controls.

Drug administration

Chloroquine was dissolved in 0.9% sterile saline and injected subcutaneously in the nape at a final concentration of 200 μg. Clozapine-N-oxide (Sigma) was dissolved in DMSO and then diluted with 0.9% sterile saline such that the concentration of DMSO did not exceed 1% of the injected solutions. For chemogenetic silencing (*R26*$^{ds\text{-}hM4Di}$) and activation (*R26*$^{ds\text{-}hM3Dq}$), experimental mice received i.p. injections of CNO (2 mg/kg of weight). *FlpO* negative mice injected with CNO were used as controls.

Chloroquine-induced scratching

Mice were acclimatized to the plexiglass chamber for 1 h for three consecutive days. On the experimental day, 200 μg of chloroquine was injected subcutaneously in the nape using a 0.5 mL insulin syringe with a 29G1/2 needle (Exel). Animals were placed in 6 cm $\times$ 6 cm x 8 cm Plexiglas boxes and video was recorded (Panasonic SDR-S26) for 30 min after injection at 30 fps. A single scratch bout was defined as every time the mouse hindlimb executed a full circular trajectory around the nape. Videos were blindly scored by the experimenter, and for each scratch episode, the time of occurrence, the duration, and number of bouts were recorded. Raster plots were generated in R using the *ggplot* package. For kinematic reconstructions, mice were injected with 200 μg of chloroquine and placed in 6 cm $\times$ 6 cm x 8 cm Plexiglas boxes for video recording using a high-speed camera (mV Blue Cougar XD; 200 frame/second). We collected 5–6 videos of 5–11 s for each mouse, sampling only a small part of the behavior, and tracked hindlimb 2D kinematics using SIMI Motion only in the videos when the scratching movement occurred perpendicularly to the camera and all the hindlimb joints/angles were visible.

Neuronal activity manipulations and behavioral testing

6- to 10-week-old mice of both sexes were used for behavioral testing following ablation or chemogenetic manipulations of neuronal activity. For ablation experiments, mice were tested 2 weeks after the first DTx injection. For CNO-induced silencing and activation, 6- to 7-week-old mice were tested 10 and 20 min following i.p. injection of the drug, respectively. All tests were conducted in the morning to minimize circadian-induced variability in response. The experimenter was blind to the genotype of the animals during the recording and the analysis of the videos and manually annotated the beginning and end of each scratch episode and the number of oscillations (bouts) of each episode. These data were used to build frequency distribution plots of the oscillations for each mouse, which were then averaged for each genotype. The kinematic trajectories were reconstructed using the pattern recognition tracking option in SIMI Motion while manually correcting the mis-tracked points. Joint coordinates were used to derive the ankle angle.

cFos expression following chloroquine-induced scratching

P56 mice were injected subcutaneously with chloroquine (200 μg) in the nape and placed in 10 cm $\times$ 10 cm plexiglass boxes. After 60 min mice were anesthetized by a single intraperitoneal (i.p.) injection (10 mL/g body weight) of solution containing 10 mg/mL ketamine and 1 mg/mL xylazine immediately prior to perfusion with 20 mL of 4% paraformaldehyde in PBS. Spinal cords were dissected and postfixed for 1 h at room temperature (RT), then rinsed 3 times in PBS and cryoprotected in 30% sucrose-PBS overnight at 4 C. Spinal cords were embedded in OCT (Tissue-Tek) and cryosectioned at 20–40 μm using a Leica CM3050 cryostat. Sections were dried at RT and stored at 20 C. Before staining OCT was removed with a 5 min PBS wash. Slides with sections were then incubated in Blocking Solution (PBS, 10% donkey serum and 0.3% Triton X-100) for 1–2 h at RT and then incubated with the primary antibody diluted as indicated in antibody solution (PBS, 1% donkey serum, 0.1% Triton X-100 and 0.025% NaN3) overnight at 4 C. Sections were then washed 3 times (15 min each) in PBT (PBS and 0.1% Triton X-100) before being incubated for 2 h at RT with antibody solution containing donkey-raised fluorophore–conjugated secondary antibodies (1:1000; Jackson Laboratories). Sections were again washed 3 times (15 min each) in PBT before being mounted with Aqua-Poly/Mount (Polysciences). A Zeiss LSM 700 confocal microscope was used to capture images.

Biophysical neuronal rate model

Neuronal populations and synaptic conductance strengths. We build a rate model[32,33,35] of a spinal cord circuit composed of interneurons and motoneurons. We assume that the neuronal populations are segregated into flexor (F) and extensor (X) modules. Each module includes an excitatory population (E), composed mostly of V2a neurons; an inhibitory population (I), composed of V1 and V2b neurons, and a motoneuron population (M). Each population is denoted by its neuronal type (first letter) and its module (second letter), and there are 6 populations: EF, IF, MF, EX, IX and MX (Figure 4A). Commissural interneuron populations are not included in the model as scratch is executed as a unilateral hindlimb movement. Anatomical and physiological evidence show that V1, V2a and V2b interneurons and motoneurons are synaptically connected,[69] although the strengths of the synaptic connections among the populations remains unknown. There is limited information on the connectivity between excitatory interneurons in one module and antagonist motoneurons, but it is well established that flexor and extensor inhibitory neurons synapse onto extensor and flexor motoneurons, respectively.[15] We neglected proprioceptive input because deafferentation (removing the sensory feedback) did not affect the scratching frequency.[70] The conductance $J^{i\alpha;j\beta}$ denotes the synaptic coupling strength from the pre-synaptic population $j\beta$ to the

post-synaptic population $i\alpha$, where $\alpha, \beta \in \{F, X\}$ and $i, j \in \{E, I, M\}$. For example, $J^{EX;IF}$ is the synaptic conductance strength from the IF population to the EX population. Based on published results,[39] we assume the excitatory conductance strength from excitatory populations (EF and EX) to be symmetrical between flexors and extensors. Under this assumption, the index for flexor/extensor can be omitted. We denote whether the conductance is "inter-" or "intra-" the flexor/extensor modules. The conductance from population EF and EX is denoted for $\alpha, \beta \in F, X$ by

$$J^{IE}_{intra} = J^{I\alpha;E\alpha}$$
$$J^{ME}_{intra} = J^{M\alpha;E\alpha} \quad \text{(Equation 1)}$$
$$J^{EE}_{inter} = J^{E\alpha;E\beta} \text{ for } \alpha \neq \beta$$

Similarly, we assume flexor and extensor symmetry between the inhibitory conductance strengths and define:

$$J^{EI}_{intra} = J^{E\alpha;I\alpha}$$
$$J^{EI}_{inter} = J^{E\alpha;I\beta} \text{ for } \alpha \neq \beta \quad \text{(Equation 2)}$$
$$J^{II}_{inter} = J^{I\alpha;I\beta} \text{ for } \alpha \neq \beta$$
$$J^{MI}_{inter} = J^{M\alpha;I\beta} \text{ for } \alpha \neq \beta$$

We consider that the excitatory neuronal populations are composed mostly by V2a neurons (proportion being $\kappa^E = 0.8$), and also include a small fraction of neurons, analogs either to Shox2-V2a neurons[7] and/or V3 neurons.[8] For inhibitory populations, we consider that V1 and V2b neurons differ in absolute numbers and innervate flexor and extensor motoneurons asymmetrically.[15] Specifically, V1 neurons are twice as many as V2b neurons (Silverman, Goulding unpublished data) and the fraction of V1 neurons is larger than the fraction of V2b neurons among the interneurons that inhibit flexor motoneurons, and vice versa for extensor (Figure S4A). This asymmetry in anatomy resulted in asymmetrical impairments of the duty cycle of flexor and extensor muscles following ablation of V1 and V2b neurons.[15] We model V1 and V2b neurons as a single I population for both flexor and extensor modules. This simplification aims to reduce the complexity of this nonlinear system, as well as to focus on a minimal circuit that could recapitulate the experimental results. In this simplified network, we model the asymmetry of V1/V2b neurons by introducing scaling parameters. We define parameters $\kappa^{I\alpha}$ to represent the relative number of V1 neurons in an α-th inhibitory population, with the relative value of V2b neurons being $1\text{-}\kappa^{I\alpha}$.

Modification of synaptic conductance strength during neuronal ablation and activation. Neuronal ablation is modeled as a reduction in the strength of the synaptic connections from a specific population. We denote the ablation efficiency of a population by p with the superscript indicating the population: V2a, V1 or V2b; $p \in [0,1]$. Therefore, the ablated connectivity from Eβ population to any population $i\alpha$ is calculated as:

$$J^{i\alpha;E\beta}_{ablated} = J^{i\alpha;E\beta}\left(\left(1 - p^{V2a}\right)\kappa^E + (1 - \kappa E)\right) \quad \text{(Equation 3)}$$

The inhibitory conductance strength after ablation of V1 or V2b neurons is calculated as:

$$J^{i\alpha;I\beta}_{ablated} = J^{i\alpha;I\beta}\left(\left(1 - p^{V1}\right)\kappa^{I\beta} + \left(1 - p^{V2b}\right)\left(1 - \kappa^{I\beta}\right)\right) \quad \text{(Equation 4)}$$

Input currents and their modification with activation. The E and I neuronal populations receive external excitatory input, mimicking input from the brain or the dorsal spinal cord. This input enables the E neurons to fire and is modeled as an external depolarizing current $I^{i\alpha}_{inp}$. Activation of a population is modeled by injecting additional activation depolarizing current to that population $I^{i\alpha}_{act}$. Therefore, the total input $I^{i\alpha}_{total}$ is

$$I^{i\alpha}_{total} = I^{i\alpha}_{inp} + I^{i\alpha}_{act} \quad \text{(Equation 5)}$$

For I populations, when either V1 or V2b neurons are activated, the input current is calculated as:

$$I^{i\alpha}_{total} = I^{i\alpha}_{inp} + I^{V1}_{act}\kappa^{I\alpha} + I^{V2b}_{act}\left(1 - \kappa^{I\alpha}\right) \quad \text{(Equation 6)}$$

Dynamics of neuronal populations. Each population is described by activation variables of the synaptic conductance $s^{i\alpha}$, firing rate $r^{i\alpha}$, adaptation current $a^{i\alpha}$ and depolarization current $d^{i\alpha}$. Synaptic facilitation is introduced into the model by setting the dynamics for facilitation variable $u^{i\alpha}$.[71] The above-mentioned variables are described by the following equations:

$$\frac{ds^{i\alpha}}{dt} = -\frac{s^{i\alpha}}{\tau^{i\alpha}_s} + u^{i\alpha}x^{i\alpha}r^{i\alpha} \quad \text{(Equation 7)}$$

$$r^{i\alpha} = \beta_r^{i\alpha}\left[I_{\text{total}}^{i\alpha} - a^{i\alpha} + d^{i\alpha} - \theta^{i\alpha} + \sum_{\substack{j=\text{E,I}\\ \beta=\text{F,X}}} J^{i\alpha;j\beta}s^{j\beta}\right]_+ \quad \text{(Equation 8)}$$

$$\frac{dd^{i\alpha}}{dt} = \frac{-d^{i\alpha} + J_d^{i\alpha}r^{i\alpha}}{\tau_d^{i\alpha}} \quad \text{(Equation 9)}$$

$$\frac{da^{i\alpha}}{dt} = \frac{-a^{i\alpha} + J_a^{i\alpha}r^{i\alpha}}{\tau_a^{i\alpha}} \quad \text{(Equation 10)}$$

$$\frac{du^{i\alpha}}{dt} = \frac{U - u^{i\alpha}}{\tau_u^{i\alpha}} + U\left(1 - u^{i\alpha}\right)r^{i\alpha} \quad \text{(Equation 11)}$$

Where $\tau_s^{i\alpha}$ are synaptic time constants, $\tau_a^{i\alpha}$ and $\tau_d^{i\alpha}$ the time constants of the adaptation and depolarization variables respectively, $\beta_s^{i\alpha}$ the slope of f-I curve (gain), $I_{\text{total}}^{i\alpha}$ the total input current to a population (Equations 5 and 6), $\theta^{i\alpha}$ the threshold current, $J^{i\alpha;j\beta}$ the synaptic conductance (Equations 2, 3, and 4), $J_a^{i\alpha}$ and $J_d^{i\alpha}$ the ratios between $a^{i\alpha}$ or $d^{i\alpha}$ and $r^{i\alpha}$ at steady state, and U the utilization of synaptic efficacy.[71] The Heavyside function $[x]_+$ (Equation 8) is defined as

$$[x]_+ = \begin{cases} 0, x \le 0 \\ x, x > 0 \end{cases} \quad \text{(Equation 12)}$$

The threshold current $\theta^{i\alpha}$ is incorporated into the default input current I_{inp}, since they are both constant. Note that the timescale for dynamics of $a^{i\alpha}$ ($\tau^{\alpha} \sim 100$ ms) is significantly larger than the timescale of $s^{i\alpha}$ ($\tau_s \sim 1$ ms). This makes the adaptation current a slow current in our model, which is essential for generating the bursting activities that were observed in experiments.[45] The values x^i are constants indicating available synaptic resource. We use the values $x^{E\alpha} = 0.92$ for excitatory neurons and $x^{I\alpha} = x^{M\alpha} = 0.48$ for inhibitory neurons and motoneurons. Equation 11 is used only for the EF and EX populations. We used the small value $U^{E\alpha} = 0.03$ to mimic strong facilitation, as shown in other systems.[35,38,72] For the other populations, $u = 0.4$ is a fixed value.

The meaning of our rate model is that the strength of an individual synapse between a population $j\beta$ and a population $i\alpha$ is $J^{i\alpha;j\beta}/K^{i\alpha;j\beta}$, where $K^{i\alpha;j\beta}$ is the average number of synaptic inputs. Therefore, if there are 1000 neurons in a population and $K^{i\alpha;j\beta} = 50$, the synaptic coupling is $J^{i\alpha;j\beta}/50$. This scaling is referred to as "mean-driven regime" or "weak coupling scenario".[63]

Parameters. The reference values of the parameter in our model are listed in Table 1 and are consistent with published datasets.[73,74]

Single module model. To illustrate functions of neural circuit components, we simulated a circuit model made up of a single module. Parameters for neuronal populations and synaptic coupling coefficients in the single module model are the same as in the full circuit, except for some of the input currents and connectivity values that are modified to account for a smaller circuit. Parameters for the model that includes E and M populations (Figures S4B–S4D) are: $J^{ME} = 130\ \mu A/cm^2$ and $I_{inp}^{E} = 0.1\ \mu A/cm^2$. Parameters for the model that includes E, I and M populations (Figures 4C and 4D, S4E, S4F) are, unless otherwise stated: $J^{IE} = 26\ \mu A/cm^2$, $J^{EI} = 10\ \mu A/cm^2$, $J^{ME} = 65\ \mu A/cm^2$, $J^{MI} = 100\ \mu A/cm^2$, and $I_{inp}^{E} = I_{inp}^{I} = 0.3\ \mu A/cm^2$.

Biomechanical model

To quantify the effects of spinal premotor interneuron manipulations on scratch frequency, we actuate a biomechanical model of the mouse ankle joint using motoneuron outputs from the neuronal model.

Link Segment Model. We model the mouse ankle joint as a one degree of freedom, two-link segment model (Figure 4B). Only the distal segment is allowed to rotate around the axis of the fixed proximal segment. The parameters used in the biomechanical model are detailed in Table 2. The y axis is parallel to the non-rotating segment, the x-axis points toward the right and the z axis points toward the reader. The unit vectors along the axes are $\hat{e}_x$, $\hat{e}_y$ and $\hat{e}_z$. The inertia of the distal segment around the axis of rotation is computed using the parallel axis theorem as:

$$I = ML_d^2/12 + Md^2, \quad \text{(Equation 13)}$$

where L_d is the length of the distal segment, M is the mass of the segment, and d is the distance from the center of mass to the axis of rotation.

The distal segment is actuated by an antagonistic pair of identical muscles. The dynamics of the distal segment's movement are described by Newton's second law as:

$$\ddot{\theta} = \frac{1}{I}\left[-\left(T_z^F + T_z^X + T_z^S\right) - B\cdot\dot{\theta}\right], \quad \text{(Equation 14)}$$

where T_z^F and T_z^X are the torques in the z direction generated by the flexor and extensor muscles respectively. The angle θ represents the ankle joint angle in radians, and $\dot{\theta}$ and $\ddot{\theta}$ denote its first and second derivatives. B defines the external viscosity, which is set to $3 \cdot 10^9$ dyn $\times$ cm $\times$ s. The fully extended ankle position is defined as $\theta = \pi$ with decreasing joint angles representing dorsiflexion, or ankle flexion. The torque from viscoelastic stops, T_z^S, is used to constrain the range of motion using the following equation:

$$T_z^S = -T_A^S \exp\left(\frac{\theta - \theta_{min}}{\sigma^S}\right) + T_A^S \exp\left(\frac{\theta_{max} - \theta}{\sigma^S}\right), \quad \text{(Equation 15)}$$

where $T_A^S = 1000$ dyn and $\sigma^S = 0.01$ rad. The maximum joint angle (i.e., the maximum plantar-flexion angle or extension), θ_{max}, is set to $0.61\ \pi$ (110°), and the minimum joint angle (i.e., the maximum flexion angle), θ_{min}, to $0.22\ \pi$ (40°).

The flexor and extensor muscles are connected in a bow-string configuration with the origin on the proximal segment $a = 1.8$ cm away from the rotation axis and the insertion on the distal segment $b = 0.1$ cm away from the rotation axis (Figure 4B).[75] The radius vector from the center of rotation O to the insertion point of the flexor muscle to the distal segment is

$$r^F = b \sin\theta\, \hat{e}_x + b \cos\theta\, \hat{e}_y \quad \text{(Equation 16)}$$

The length of the flexor muscle is

$$L^F = \left(a^2 - 2ab\cos\theta + b^2\right)^{1/2} \quad \text{(Equation 17)}$$

The vector force of the flexor muscle is

$$\vec{F}^F = F^F \frac{-b\sin\theta\, \hat{e}_x + (a - b\cos\theta)\hat{e}_y}{\left(a^2 - 2ab\cos\theta + b^2\right)^{1/2}} \quad \text{(Equation 18)}$$

The torque of the flexor muscle is

$$\vec{T}^F = F^F \frac{ab\sin\theta}{\left(a^2 - 2ab\cos\theta + b^2\right)^{1/2}} \hat{e}_z \quad \text{(Equation 19)}$$

For the torque generated by the extensor muscle, a calculation similar to Equations 16, 17, 18, and 19 applies when $\theta > \theta_c = -\arccos(b/a)$, which corresponds to 1.63 rad (93.2°) for our parameter set. The length of the extensor muscle is calculated as

$$L^X = \left(a^2 + 2ab\cos\theta + b^2\right)^{1/2} \quad \text{(Equation 20)}$$

The torque of the extensor muscle as

$$\vec{T}^X = F^X \frac{-ab\sin\theta}{\left(a^2 + 2ab\cos\theta + b^2\right)^{1/2}} \hat{e}_z \quad \text{(Equation 21)}$$

For $\theta < \theta_c$

$$L^X = \left(a^2 - b^2\right)^{1/2} + b(\theta_c - \theta) \quad \text{(Equation 22)}$$

$$\vec{T}^X = -F^X b \hat{e}_z \quad \text{(Equation 23)}$$

Note that "muscle length" here means the total length of the musculotendon unit, i.e., the muscle fiber length (L_m^α) plus the tendon/aponeurosis length (L_t^α) for α = F,X. For simplicity, we assume inflexible tendon/aponeurosis and therefore length changes are all taken up by muscle fibers. The optimal musculotendon length (the length of the musculotendon for which the active force is maximal) is taken to be $L_0 = 0.473$ cm for both muscles.[75] The maximal allowed length of the musculotendon is defined as $\alpha_L L_0$ where $\alpha_L = 1.1$. Therefore, the length of the tendon of the flexor is $L_t^F = L_F(\theta_{max}) - \alpha_L L_0 = 0.0131$ cm (Equation 17) and that of the extensor is $L_t^X = L_X(\theta_{min}) - \alpha_L L_0 = 0.0137$ cm (Equation 22). As the total muscle length $L^\alpha(t)$ varies, the length of the musculotendon unit $L_m^\alpha(t)$ is

$$L_m^\alpha(t) = L^\alpha(t) - L_t^\alpha(t) \quad \text{(Equation 24)}$$

Muscle Model. A muscle model converts motoneuron activity, r^{MF} and r^{MX}, and muscle lengths into muscle forces, F_m^F and F_m^X, respectively. In addition to the low-pass filtering effects of muscle, we include the following known muscle properties: the length-dependent muscle activation, force-length relationship, and a passive elastic element. These properties are added to prevent drift in joint angles that would otherwise occur in a linear muscle model. Both flexor and extensor muscles are modeled identically to reduce the complexity of the model.

Muscle force. The muscle force (F_m) comprises forces from an active contractile element (F_{CE}), and a passive elastic element (F_{PE}) (Figure S7A). F_{CE} and F_{PE} are represented as a fraction of the muscle force, F_0

$$F_m = (F_{CE} + F_{PE}) \cdot F_0 \quad \text{(Equation 25)}$$

The maximum muscle force F_0 is set to $2.13 \cdot 10^5$ dyn for both muscles.[75]

Passive elastic element. The model includes a passive elastic element situated parallel to the contractile element. This passive elasticity arises from connective tissues within the muscle.[42] The force generated by this passive element, F_{PE}, increases with the muscle fiber length (Figure S7B)[76]:

$$F_{PE}(L) = c_1 k_1 \ln\left[\exp\left(\frac{L_{m,norm}/\alpha_L - L_{r1}}{k_1}\right) + 1\right] \quad \text{(Equation 26)}$$

where the normalized musculotendon length is (Equation 24)

$$L_{m,norm} = \frac{L_m^{\alpha}}{L_0} = \frac{L - L_t}{L_0} \quad \text{(Equation 27)}$$

The parameters k_1 and L_{r1} are obtained from Song et al.[76] The value of c_1, which defines the asymptotic slope of the exponential function (i.e., stiffness), is adjusted to be 6 times larger than in the original model[76] to account for the higher passive stiffness of the mouse muscle.[77,78]

Resting muscle length and joint angle. The resting joint angle θ_{rest} is the angle θ for which $\dot{\theta} = 0$ and $\ddot{\theta} = 0$ for zero active force. Assuming it is not near θ_{min} or θ_{max},

$$T_z^F + T_z^X = 0 \quad \text{(Equation 28)}$$

for $\theta = \theta_{rest}$ and $F_{CE} = 0$ (Equation 14). We solved Equations 18, 19, 21, 23, and 26 and obtained $\theta_{rest} = 1.31$ rad (75°). This angle, together with $\dot{\theta} = 0$, is used as the initial condition for simulations.

Active force. The amount of active force depends on the level of muscle activation, A, as well as the activation-dependent force-length relationship of the contractile element, A_f and A_{FL}:

$$F_{CE} = A \cdot A_F \cdot A_{FL} \quad \text{(Equation 29)}$$

Muscle activation. Neuronal excitation (i.e., the activity of motoneurons) results in the activation of cross-bridges within muscle fibers that can participate in active force generation, which we refer to as muscle activation $A^{\alpha}(t)$; $\alpha = F, X$. We used a model of second-order dynamics[79] to relate $A^{\alpha}(t)$ to the motoneuron firing rate $r^{M\alpha}(t)$

$$\tau_{A1}\tau_{A2}\ddot{A^{\alpha}}(t) + (\tau_{A1} + \tau_{A2})\dot{A^{\alpha}}(t) + A^{\alpha}(t) = \tanh\left(\frac{r^{M\alpha}(t)}{r_0}\right), \quad \text{(Equation 30)}$$

where $r^{M\alpha}(t)$ is the population-average firing rate of the α-th motoneuron pool (Equation 8). and $r_0 = 54$ Hz is a normalization constant. The tanh function in Equation 30 ensures that the normalized neural input to the muscle model is less than 1. $A^{\alpha}(t)$ denotes muscle activation, which ranges from 0 to 1. This second-order differential equation captures the low-pass filtering effect of muscle,[80] arising from the biophysical properties of muscle force generation. τ_{A1} and τ_{A2} are set to 10 ms to account for the faster contraction capability of mouse muscles compared to humans and other animals.[81]

Force-length relationship. The maximum amount of force a muscle can generate depends on its fiber length, known as the force-length relationship. This relationship scales muscle force as a function of the normalized muscle fiber length, $L_{m,norm}$ (Equation 27).[76] The force-generating capability of a muscle decreases when the muscle becomes longer or shorter than its optimal muscle fiber length ($L_{m,norm} = 1$)[42,82]. This property is thought to arise from the extent of myofilament overlap at different muscle lengths.[83] This nonlinear relationship is modeled by scaling muscle force by A_{FL}[76]:

$$A_{FL} = \exp\left[-\left|\frac{L_{m,norm}^{\beta_{FL}} - 1}{\omega}\right|^{\rho}\right] \quad \text{(Equation 31)}$$

where the values of model parameters, ω, β_{FL}, and ρ (Table 2) are those for fast-twitch units.[76]

We also included the dependence of muscle activation on muscle fiber length previously reported for mammalian skeletal muscles[43] (Figure S7C). This is thought to arise from mechanisms independent of myofilament overlap such as changes in the rate of cross-bridge formation and detachment.[43] We model this by adding a scaling factor, A_f, to muscle activation, whose value ranges from 0 to 1 (Equation 29).

$$A_f = 1 - \exp\left[-\left(\frac{f_{eff}}{\alpha_f n_f}\right)^{n_f}\right], \quad \text{(Equation 32)}$$

$$n_f = n_{f0} + n_{f1}\left(\frac{1}{L_{\mathrm{m,norm}}} - 1\right)$$

where

$$f_{\mathrm{eff}} = 1.5A + 0.5 \quad \text{(Equation 33)}$$

The parameters a_f, n_{f0} and n_{f1}, are taken from those for fast-twitch units in the original model.[43] The total muscle-length curve is $A_f \cdot A_{\mathrm{FL}}$ (Figure S7C).

Calculation of oscillation frequency and identification of dynamics categories

Frequency calculation. We use the function *find_peaks* in the python package *scipy.signal* to identify peaks in the simulated dynamics of MF and MX firing, as well as in the simulated joint angles. The number of peaks within a time interval T_{interval} is noted as N_{peaks} with a superscript "F", "X" or "movement", corresponding to peaks in r^{MF}, r^{MX} and θ, respectively. We defined the movement frequency as the number of joint movements varying more than ±5° from the balanced angle position (75°) per time unit, in sequences of "flexor-extensor" or "extensor-flexor" movements: $f_{\mathrm{movement}} = N_{\mathrm{peaks}}^{\mathrm{movement}} / T_{\mathrm{interval}}$. Therefore, if the movement does not reach 5° in both directions, the joint is not considered to be oscillating (Figures 6F and 6G).

A diversity of motoneuron dynamics emerges in our simulations. We divide the temporal dynamical states into four categories. In addition to regular, periodic firing, there are states of irregular oscillations, 100% co-contraction and atonia. Except during atonia, we compute the range of peak heights during a large time interval.

Regular oscillations (Figures 4G–4J) are characterized by periodic (15 seconds) oscillations with a non-zero phase difference between the MF and MX populations, and by the range of peak heights (difference between maximum and minimum peak heights) being less than 5% smaller than the mean. Phase difference ϕ (Figures S5E and S5F) was computed only for regular oscillations. It is defined as the ratio of the time interval between adjacent MF and MX peaks to the oscillation period, under the assumption that MF and MX share the same period in regular oscillations.

Irregular oscillations (Figures S4J and S4K) are states in which the range of peak heights is 5% larger than the mean. The dynamics may be aperiodic.

In *100% co-contraction* states (Figures S4L and S4M), the MF and MX populations oscillate in phase and simultaneously reached their maximal value, leading to the joint angle being stuck or flexed or extended only in one direction. The dynamics are periodic and regular.

Atonia (Figures S4N and S4O) refers to a fixed point in the dynamical system, where its variables, including MF and MX, are constant with time.

Co-contraction rate calculation. Besides 100% co-contraction states, partial co-contractions also happen in irregular oscillation states, during which some but not all MF/MX peaks oscillate in phase and simultaneously reach their maximal value (Figure S4J). To quantify the effects of ablation or activation of neuronal populations on the occurrence of co-contraction, we define co-contraction rate $r^{\mathrm{co\text{-}contract}}$ (Figure 6I) as

$$r^{\mathrm{co-contract}} = \frac{N_{\mathrm{peaks}}^{\mathrm{co-contract}}}{N_{\mathrm{peaks}}^{\mathrm{total}}} \quad \text{(Equation 34)}$$

where $N_{\mathrm{peaks}}^{\mathrm{co-contract}}$ is the number of peaks in which MF and MX populations oscillate in phase and simultaneously reach their maximal values, and $N_{\mathrm{peaks}}^{\mathrm{total}}$ is the total number of peaks. During irregular oscillations, due to asymmetry, $N_{\mathrm{peaks}}^{\mathrm{total}}$ can be different for MF and MX, in such case we define $N_{\mathrm{peaks}}^{\mathrm{total}} = \min\left(N_{\mathrm{peaks}}^{\mathrm{F}}, N_{\mathrm{peaks}}^{\mathrm{X}}\right)$. The value $r^{\mathrm{co\text{-}contract}}$ can be equivalently calculated from joint angle dynamics as $N_{\mathrm{peaks}}^{\mathrm{co-contract}} = N_{\mathrm{peaks}}^{\mathrm{total}} - N_{\mathrm{peaks}}^{\mathrm{movement}}$. We categorize trials with $r^{\mathrm{co\text{-}contract}} > 0.99$ as "100% co-contraction".

Simulations and visualization

Numerical methods. Simulations of the neuro-mechanical model are performed using Euler's method with time step $\Delta t = 0.1$ ms.

Simulations with random distributed connectivity values. For each tested parameter set, we repeated the simulations for 50 realizations with the values of synaptic conductance coefficients generated from a uniform distribution ranging between ±10% of their assigned value (Table 1).

The computed values of a variable, such as oscillation frequency or phase difference between motoneuron populations, are plotted in graphs as mean ± standard deviation (SD). There are cases in which there is almost no variability in the computed values despite variation in parameter set. For example, there is almost no variability in the phase difference between the flexor and extensor motoneuron populations (MF and MX) for V1 or V2b neuron ablation efficiency above 0.30 (Figure S5F). This lack of variability is explained by the fact that bursting activity of one population occurs just after the activity of the other population. For example, the phase difference in Figure 4I (but not in Figure 4G) is dictated by the width of the burst.

Initial conditions. For each realization of random connectivity values, the first simulation started with the following initial values: $a^{i\alpha}(0) = 0.5\ \mu$A/cm,^{2} $d^{i\alpha}(0) = 0\ \mu$A/cm,^{2} $u^{\mathrm{E}\alpha}(0) = 0.1$, $s^{\mathrm{M}\alpha}(0) = s^{\mathrm{EX}}(0) = s^{\mathrm{IX}}(0) = 0.01$, $s^{\mathrm{EF}}(0) = 0.011$, $s^{\mathrm{IF}}(0) = 0.012$. The initial values of

$s^{i\alpha}$ are chosen to introduce a slight asymmetry between flexor and extensor at initialization, but the attractor dynamics are not sensitive to the choice of this asymmetry. Unless otherwise stated, trials following the first simulation are simulated using the final state of the last simulation as initial conditions.

Computing the fractions of various dynamical categories. Each simulated trial is categorized as regular, irregular, 100% co-contraction or atonia (only in V1 or V2b neuron activation case). The fraction of each dynamical category among the 50 realizations is computed. Only categories with fractions larger than 14% (7 out of 50 realizations) are plotted to ensure the generation of a sufficient amount of data to compute the statistics.

Fourier analysis. To illustrate how the irregularity in oscillations changed following perturbations of population activity, Fourier spectrum of the joint angle dynamics is computed using *scipy.fft.rfft*. For each figure panel, a Fourier spectrum is computed for a randomly selected trial from the realizations.

QUANTIFICATION AND STATISTICAL ANALYSIS

All statistical analyses were done in Prism. Depending on the number of groups and variables to compare, we used two-way ANOVA with Bonferroni's post hoc test, or two-tailed unpaired Student's t-test as indicated in the figure legend.